Adv Comput Math (2020) 46:25
https://doi.org/10.1007/s10444-020-09764-4

Discontinuous finite volume element method for a coupled Navier-Stokes-Cahn-Hilliard phase field model

Rui Li[1] · Yali Gao[2] · Jie Chen[3] · Li Zhang[4] · Xiaoming He[5] · Zhangxin Chen[6]

Received: 20 January 2019 / Accepted: 23 January 2020 / Published online: 14 March 2020

Abstract
In this paper, we propose a discontinuous finite volume element method to solve a phase field model for two immiscible incompressible fluids. In this finite volume element scheme, discontinuous linear finite element basis functions are used to approximate the velocity, phase function, and chemical potential while piecewise constants are used to approximate the pressure. This numerical method is efficient, optimally convergent, conserving the mass, convenient to implement, flexible for mesh refinement, and easy to handle complex geometries with different types of boundary conditions. We rigorously prove the mass conservation property and the discrete energy dissipation for the proposed fully discrete discontinuous finite volume element scheme. Using numerical tests, we verify the accuracy, confirm the mass conservation and the energy law, test the influence of surface tension and small density variations, and simulate the driven cavity, the Rayleigh-Taylor instability.

Keywords Phase field model · Navier-Stokes-Cahn-Hilliard equation · Discontinuous finite volume element methods · Discrete energy dissipation

Mathematics subject classification (2010) 65M12 · 76M12 · 76D05 · 76TXX

1 Introduction

The phase field method, whose basic idea dates back to the pioneering work of [82, 90], has been widely utilized as one of the major tools to study a variety of interfacial phenomena. This method uses an auxiliary variable $\varphi(\boldsymbol{x}, t)$ to localize the phases

Communicated by: Ilaria Perugia

✉ Yali Gao
gaoyli2008@163.com

Extended author information available on the last page of the article.

and describe the interface by a layer of small thickness. This phase function takes two different values (such as $+1$ and -1) in the two phases and varies smoothly across the interface, i.e., in the phase field model, the interface is considered as a transition layer over which a continuous, but steep change of some physical quantities occur. The phase field models can be naturally derived from variational principle, i.e., via minimizing the free energy of the total system. As a result, the derived system satisfies an energy dissipation law, which justifies its thermodynamic consistency and leads to a mathematically well-posed model [4, 27, 64].

Moreover, the presence of the energy law serves as a guide line for the design of energy stable numerical schemes. Various numerical methods have been developed and analyzed for different phase field models, such as the finite element method [3, 30, 35, 40, 45, 52, 54, 100], finite difference method [14, 16, 99], spectral method [46, 67, 87, 91, 102], extended finite element method [18, 32], discontinuous Galerkin finite element method [31, 66, 84], finite volume method [7, 106], penalty-projection method [83], lattice Boltzmann method [26, 107], and many others [13, 50, 53, 63, 71, 77, 79, 80, 98, 105].

Practitioners often prefer to utilize low-order finite elements, such as P_0 and P_1 elements, since they are simple to implement and can provide enough accuracy for many applications. However, the regular Galerkin method with $P_1 - P_0$ and $P_1 - P_1$ finite element pairs is not stable for the Navier-Stokes equations since they do not satisfy the inf-sup condition [36, 38, 89]. On the other hand, for velocity and pressure approximation, the discontinuous Galerkin formulation with $P_1 - P_0$ space is stable [85]. Because of its flexibility for mesh/polynomial refinement, localizability, and stability, the discontinuous Galerkin method has been widely extended and applied to solve many partial differential equations, such as the local discontinuous Galerkin (LDG) method [17, 22, 51, 97], the interior penalty discontinuous Galerkin (IPDG) method [1, 24, 25, 78, 86, 96, 101], the hybridizable DG method [10, 20, 43, 48, 76], reduced order DG method [58–60], and many others [15, 49, 61, 68, 72–74, 81, 92, 95, 108]. One important feature of the IPDG method is its capability to easily incorporate *hp* local refinement. Therefore, it is natural to apply them to phase field problems since local refinement is usually needed around an interface.

To the author's best knowledge, this article is the first work to develop and analyze the discontinuous finite volume element (DFVE) method for the coupled Cahn-Hilliard and Navier-Stokes equations. DFVE method has the flexibility in mesh refinement, the optimal order of accuracy, the conservative property, the capability to handle complex geometries, and the advantage of convenient implementation, due to the combination of the advantages of the finite volume element method and interior penalty discontinuous Galerkin method. The fascinating nature of DFVE method reflects on the smaller conservation control volume which is less than half the size of control volume applied in the existing FVE methods. Another attractive feature is the block diagonal mass matrices in the context of the time-dependent problems. The localizability of the discontinuous element and its dual partition in DFVE method also benefit parallel computation. Therefore, the DFVE method has attracted scientists and engineers for different equations, such as the second-order elliptic problems [9, 19, 56, 70, 103], Stokes equation [23, 94, 104], some non-linear problems [8, 55, 57], and several multi-physics coupled problems [62, 93]. DFVE method has also

been used to solve elliptic problem with adaptive technique and other applications [69, 75].

The paper is organized as follows: in Section 2, we briefly introduce the Navier-Stokes-Cahn-Hilliard model and its weak formulation; in Section 3, the fully discrete discontinuous finite volume element methods are presented and analyzed for mass conservation and energy dissipation properties; in Section 4, a series of numerical experiments are provided; finally, conclusions are presented in Section 5.

Throughout the paper, the letter C denotes a generic positive constant, which is different in different lines but independent of the mesh size.

2 Navier-Stokes-Cahn-Hilliard model

We consider a model describing the motion of a mixture of two viscous fluids with matching density (or almost matching density), and same dynamic viscosity in a bounded domain. The fluids are assumed to be immiscible and incompressible. A phase function $\varphi(\boldsymbol{x}, t)$ is used to identify the two Newtonian fluids, namely

$$\varphi(\boldsymbol{x}, t) = \begin{cases} 1 & \text{fluid 1}, \\ -1 & \text{fluid 2}, \end{cases} \tag{1}$$

with a thin, smooth transition region of width between the two fluids. Hence, the interface between the two phases is described by the zero level set $\Gamma_t = \{\boldsymbol{x} : \varphi(\boldsymbol{x}, t) = 0\}$.

Here, we consider the following coupled Navier-Stokes-Cahn-Hilliard equation in two-dimensional domains

$$\mathcal{R}(\mathbf{u}_t + (\mathbf{u}\cdot\nabla)\mathbf{u}) - \Delta\mathbf{u} + \nabla p - \mathcal{B}w\nabla\varphi = \mathbf{f} \quad \text{in} \quad \Omega, \tag{2}$$

$$\nabla\cdot\mathbf{u} = 0 \quad \text{in} \quad \Omega, \tag{3}$$

$$\varphi_t + \mathbf{u}\cdot\nabla\varphi - L_d\Delta w = 0 \quad \text{in} \quad \Omega, \tag{4}$$

$$w + \varepsilon\Delta\varphi - \frac{1}{\varepsilon}f(\varphi) = 0 \quad \text{in} \quad \Omega, \tag{5}$$

where $\mathbf{u}$ is the velocity, p is the pressure, w is the chemical potential, $\mathbf{f}$ is an additional gravitational force, and $f(\varphi)$ is the first derivative of a double well potential $F(\varphi)$. That is, $f(\varphi) = F'(\varphi)$ and $F(\varphi)$ is the truncated double well potential

$$F(\varphi) = \begin{cases} (\varphi+1)^2 & \text{if } \varphi \in (-\infty, -1], \\ \frac{1}{4}(\varphi^2-1)^2 & \text{if } \varphi \in [-1, 1], \\ (\varphi-1)^2 & \text{if } \varphi \in [1, +\infty). \end{cases} \tag{6}$$

There are four non-dimensional parameters in this system. $\mathcal{R}$ is the Reynolds number, $\mathcal{B}$ denotes the strength of the capillary force comparing with the Newtonian fluid stress, L_d is the (constant) mobility, and ε is the ratio between interface thickness and domain size. We note that the equations (4)–(5) differ from the original Cahn-Hilliard equation [28], the chemical potential $w = -\varepsilon\Delta\varphi + \frac{1}{\varepsilon}f(\varphi)$ is used by Feng [29] and Han [39, 41]. Similar parameters are used by He [42], Chen [11], and Gao [33, 34], with ε and L_d here denoted by the Cahn number Ca and the inverse of a Péclet nmuber $\frac{1}{Pe}$ in [79, 80], correspondingly. In this case, $M = 1$ holds for the mobility.

We close the system with the following initial and boundary conditions:

$$\mathbf{u}(\cdot,0)=\mathbf{u}_0,\quad \varphi(\cdot,0)=\varphi_0 \qquad \text{in}\quad \Omega, \tag{7}$$

$$\mathbf{u}=0,\quad \frac{\partial\varphi}{\partial\mathbf{n}}=\frac{\partial w}{\partial\mathbf{n}}=0 \qquad \text{on}\quad \Gamma\times(0,T]. \tag{8}$$

Next, we present the weak formulation for this model. Let B^* denote the dual space of a Banach space B and $(\cdot,\cdot)$ denote the standard $L^2(\Omega)$ inner product. Define the Hilbert spaces

$$\begin{aligned}
&\mathbf{V}(\Omega)=\{\mathbf{v}\in\mathbf{H}_0^1(\Omega);\ \nabla\cdot\mathbf{v}=0 \text{ in } \Omega\},\\
&\mathbf{H}(\Omega)=\{\mathbf{v}\in\mathbf{L}^2(\Omega);\ \nabla\cdot\mathbf{v}=0 \text{ in } \Omega \text{ and } \mathbf{v}\cdot\mathbf{n}=0 \text{ on } \Gamma\},\\
&L_0^2(\Omega)=\{q\in L^2(\Omega);\ (q,1)=0\}.
\end{aligned}$$

In particular, we use the notation for the norm and the seminorm hereafter:

$$\|\cdot\|:=\|\cdot\|_{L^2(\Omega)},\qquad |\cdot|_1:=\|\nabla\cdot\|_{L^2(\Omega)}.$$

The mixed weak formulation of (2)–(8) is defined as follows [30]: find $(\mathbf{u},p,\varphi,w)$ with

$$\begin{aligned}
&\mathbf{u}\in L^\infty((0,T),\mathbf{L}^2(\Omega))\cap L^2((0,T),\mathbf{H}_0^1(\Omega))\cap H^1((0,T),\mathbf{V}^*(\Omega)),\\
&p\in L^\infty((0,T),L_0^2(\Omega)),\\
&\varphi\in L^\infty((0,T),H^1(\Omega))\cap H^1((0,T),\mathbf{H}^{-1}(\Omega)),\\
&w\in L^2((0,T),H^1(\Omega)),
\end{aligned}$$

such that for all $(\mathbf{v},q,\psi,\chi)\in\mathbf{V}(\Omega)\times L_0^2(\Omega)\times H^1(\Omega)\times H^1(\Omega)$ there hold

$$\mathcal{R}(\mathbf{u}_t,\mathbf{v})+(\nabla\mathbf{u},\nabla\mathbf{v})+\mathcal{R}((\mathbf{u}\cdot\nabla)\mathbf{u},\mathbf{v})-(p,\nabla\cdot\mathbf{v})-\mathcal{B}(w\nabla\varphi,\mathbf{v})=(\mathbf{f},\mathbf{v}), \tag{9}$$

$$(\nabla\cdot\mathbf{u},q)=0, \tag{10}$$

$$(\varphi_t,\psi)+(\mathbf{u}\cdot\nabla\varphi,\psi)+L_d(\nabla w,\nabla\psi)=0, \tag{11}$$

$$(w,\chi)-\varepsilon(\nabla\varphi,\nabla\chi)-\left(\frac{1}{\varepsilon}f(\varphi),\chi\right)=0, \tag{12}$$

with the initial conditions $\mathbf{u}(\cdot,0)=\mathbf{u}_0$ and $\varphi(\cdot,0)=\varphi_0$.

An important feature of the above weak formulation is that it obeys a dissipative energy law. We denote the total energy of the coupled system as:

$$E(t;\mathbf{u},\varphi)=\int_\Omega\frac{\mathcal{R}}{2}\mathbf{u}^2\,\mathrm{d}\boldsymbol{x}+\mathcal{B}\int_\Omega\left(\frac{\varepsilon}{2}\nabla\varphi\cdot\nabla\varphi+\frac{1}{\varepsilon}F(\varphi)\right)\mathrm{d}\boldsymbol{x}. \tag{13}$$

We recall the following lemma about the basic energy law from [30, 47].

Lemma 2.1 *Let $(\mathbf{u},p,\varphi,w)$ be a smooth solution to the initial boundary value problem (2)–(8). Assume that $\mathbf{f}=\mathbf{0}$, then this system has the following basic energy law:*

$$\tfrac{d}{dt}E(t;\mathbf{u},\varphi)=-\mathcal{D}(t;\mathbf{u},w), \tag{14}$$

where the energy dissipation $\mathcal{D}(t;\mathbf{u},w)$ is given by

$$\mathcal{D}(t;\mathbf{u},w)=\int_\Omega[\nabla\mathbf{u}:\nabla\mathbf{u}+\mathcal{B}L_d\|\nabla w\|^2]\,\mathrm{d}\boldsymbol{x}. \tag{15}$$

3 Discontinuous finite volume element method

Let $\mathcal{R}_h$ be a regular triangular partition of Ω and h_K be the diameter of the triangle $K \in \mathcal{R}_h$. The triangles $K \in \mathcal{R}_h$ are divided into three subtriangles T by connecting the barycenter of the triangle K to its corner nodes, then we define the dual partition $\mathcal{T}_h$ of the primal partition $\mathcal{R}_h$ to be the union of the triangles T as shown in Fig. 1. Define the mesh parameter $h = \max_{K \in \mathcal{T}_h} h_K$. The length of edge e in element K is denoted by h_e, the set of all interior edges e in $\mathcal{R}_h$ is denoted by $\mathcal{E}^o$, the set of all boundary edges belong to Dirichlet boundary in $\mathcal{R}_h$ is denoted by $\mathcal{E}^D$, and the set of all boundary edges belonging to Neumann boundary in $\mathcal{R}_h$ is denoted by $\mathcal{E}^N$. Hence, we have $\mathcal{E}_{\mathbf{u}} = \mathcal{E}^o \cup \mathcal{E}^D$, $\mathcal{E}_{\varphi} = \mathcal{E}^o \cup \mathcal{E}^N$, and $\mathcal{E}_w = \mathcal{E}^o \cup \mathcal{E}^N$.

Let $P_k(T)$ consist of all the polynomials with degree less than or equal to k defined on T. Define the finite dimensional trial function space for velocity on triangular partition:

$$\mathbf{X}_h = \left\{ \mathbf{v} \in (L^2(\Omega))^2 : \mathbf{v}|_K \in (P_1(K))^2, \ \forall K \in \mathcal{R}_h \right\}.$$

Define the finite dimensional test function space $\mathbf{X}_h^*$ for velocity associated with the dual partition $\mathcal{T}_h$:

$$\mathbf{X}_h^* = \left\{ \mathbf{v} \in (L^2(\Omega))^2 : \mathbf{v}|_T \in (P_0(T))^2, \ \forall T \in \mathcal{T}_h \right\}.$$

Let M_h be the finite dimensional space for pressure:

$$M_h = \left\{ q \in L_0^2(\Omega) : q|_K \in P_0(K), \ \forall K \in \mathcal{R}_h \right\}.$$

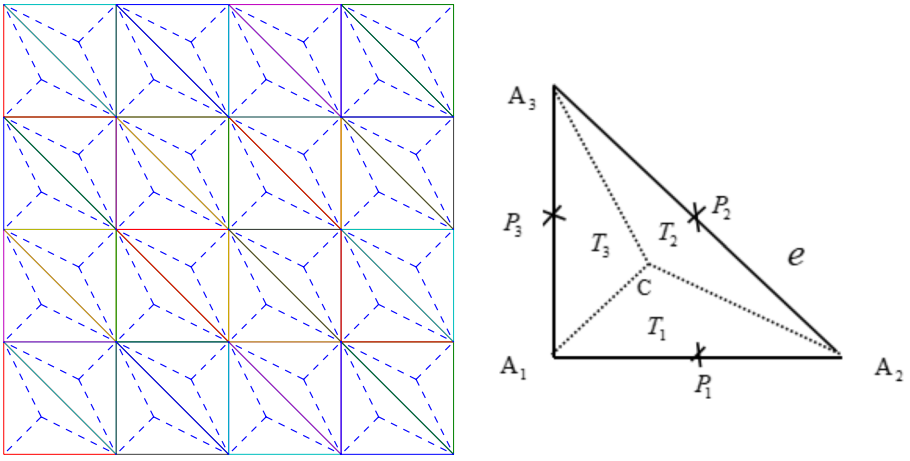

Fig. 1 Left: An example of primal mesh (solid lines) and its dual mesh (dashed lines); Right: An element K and its dual element T_j, P_j is the midpoint of every edge, $j = 1, 2, 3$

Define trial function space Y_h and test function space Y_h^* for phase field variable φ:

$$Y_h = \left\{\psi \in L^2(\Omega) : \psi|_K \in P_1(K),\ \forall K \in \mathcal{R}_h\right\},$$
$$Y_h^* = \left\{\psi \in L^2(\Omega) : \psi|_T \in P_0(T),\ \forall T \in \mathcal{T}_h\right\}.$$

Define trial function space G_h and test function space G_h^* for chemical potential variable w:

$$G_h = \left\{\chi \in L^2(\Omega) : \chi|_K \in P_1(K),\ \forall K \in \mathcal{R}_h\right\},$$
$$G_h^* = \left\{\chi \in L^2(\Omega) : \chi|_T \in P_0(T),\ \forall T \in \mathcal{T}_h\right\}.$$

It is well known [8, 37, 85, 104] that the discontinuous finite element space $(\mathbf{X}_h, M_h)$ is a stable pair for the Navier-Stokes equations since it satisfies the inf-sup condition. That is, there exists a constant $\beta_1 > 0$ such that

$$\inf_{0\neq q_h\in M_h}\sup_{\mathbf{0}\neq\mathbf{v}_h\in\mathbf{X}_h}\frac{(q_h, \nabla\cdot\mathbf{v}_h)}{\|q_h\|_0\|\mathbf{v}_h\|_1} \geq \beta_1. \tag{16}$$

It is also well known [29, 65] that (Y_h, G_h) is a stable pair for the biharmonic operator and there holds the inf-sup condition, that is, there exists a constant $\beta_2 > 0$ such that

$$\inf_{0\neq\chi_h\in G_h}\sup_{0\neq\psi_h\in Y_h}\frac{(\nabla\psi_h, \nabla\chi_h)}{\|\chi_h\|_1\|\psi_h\|_1} \geq \beta_2. \tag{17}$$

For vectors $\mathbf{v}$ and $\mathbf{n}$, let $\mathbf{v}\otimes\mathbf{n}$ be the matrix whose ijth component is $v_i n_j$ as in [21]. For two matrix valued variables σ and δ, we define $\sigma : \delta = \sum_{i,j=1}^2 \sigma_{ij}\delta_{ij}$. An interior edge shared by two elements K_1 and K_2 in $\mathcal{T}_h$ is denoted by e, and the unit normal vectors on e pointing exterior to K_1 and K_2 are denoted by $\mathbf{n}_1$ and $\mathbf{n}_2$, respectively. We define the average $\{\cdot\}$ and jump $[\cdot]$ on e for a function φ, and φ can be scalar q, vector $\mathbf{v}$ and matrix δ.

$$\{\varphi\} = \frac{1}{2}(\varphi|_{\partial K_1} + \varphi|_{\partial K_2}), \quad [\varphi] = \varphi|_{\partial K_1}\mathbf{n}_1 + \varphi|_{\partial K_2}\mathbf{n}_2.$$

If e is an edge on the boundary of Ω, define: $\{q\} = q$, $[\mathbf{v}] = \mathbf{v}\cdot\mathbf{n}_\Omega$, $\{\tau\} = \tau$.

Let $\mathcal{E}$ denote the union of the boundaries of the triangles K of $\mathcal{R}_h$ and $\mathcal{E}_0 := \mathcal{E}\backslash\partial\Omega$. A straightforward computation implies

$$\sum_{K\in\mathcal{R}_h}\int_{\partial K} q\mathbf{v}\cdot\mathbf{n}_K\,\mathrm{d}s = \sum_{e\in\mathcal{E}_0}\int_e [q]\cdot\{\mathbf{v}\}\,\mathrm{d}s + \sum_{e\in\mathcal{E}}\int_e \{q\}\,[\mathbf{v}]\,\mathrm{d}s, \tag{18}$$

$$\sum_{K\in\mathcal{R}_h}\int_{\partial K} \mathbf{v}\cdot\tau\mathbf{n}_K\,\mathrm{d}s = \sum_{e\in\mathcal{E}_0}\int_e [\tau]\cdot\{\mathbf{v}\}\,\mathrm{d}s + \sum_{e\in\mathcal{E}}\int_e \{\tau\} : [\mathbf{v}]\,\mathrm{d}s, \tag{19}$$

where $\mathbf{n}_K$ is the unit outward normal vector on ∂K.

Let $\mathbf{X}(h) = \mathbf{X}_h + (H^2(\Omega))^2\cap\mathbf{V}(\Omega)$, $Y(h) = Y_h + H^2(\Omega)$, $G(h) = G_h + H^2(\Omega)$. In order to connect $\mathbf{X}_h$ to $\mathbf{X}_h^*$, Y_h to Y_h^* and G_h to G_h^*, respectively, we define the projection maps $\gamma : \mathbf{X}(h) \to \mathbf{X}_h^*$, $\gamma : Y(h) \to Y_h^*$ and $\gamma : G(h) \to G_h^*$ as follows:

$$\gamma\mathbf{v}|_T = \frac{1}{h_e}\int_e \mathbf{v}|_T\,\mathrm{d}s, \quad \gamma\varphi|_T = \frac{1}{h_e}\int_e \varphi|_T\,\mathrm{d}s, \quad \gamma w|_T = \frac{1}{h_e}\int_e w|_T\,\mathrm{d}s, \quad T \in \mathcal{T}_h.$$

where e is defined as $\partial K \bigcap \partial T$.

We recall the following lemma about projection operator γ from [6, 19].

Lemma 3.1 *If $\mathbf{v}_h \in \mathbf{X}_h$, $K \in \mathcal{R}_h$, then*

$$\int_K (\mathbf{v}_h - \gamma \mathbf{v}_h)\,\mathrm{d}\boldsymbol{x} = 0, \qquad \int_e (\mathbf{v}_h - \gamma \mathbf{v}_h)\,\mathrm{d}s = 0, \quad \forall e \in \partial K,$$
$$\|\|\gamma \mathbf{v}_h - \mathbf{v}_h\|_K \le C h_K |\mathbf{v}_h|_{1,T}, \qquad [\gamma \mathbf{v_h}] = \frac{1}{h_e}\int_e [\mathbf{v}_h]\,\mathrm{d}s,$$
$$\|\|[\gamma \mathbf{v_h}]\|_e \le \|[\mathbf{v}_h]\|_e, \qquad \|\gamma v_h\|_0 = \|v_h\|_0.$$

And these conclusions are also true for the variables $\varphi \in Y_h$ and $w \in Y_h$.

Note that the operator γ is self-adjoint with respect to the L^2 inner product, i.e.,

$$(\mathbf{v}_h, \gamma \mathbf{u}_h) = (\mathbf{u}_h, \gamma \mathbf{v}_h), \quad \forall \mathbf{u}_h, \mathbf{v}_h \in \mathbf{X}_h, \quad (\varphi_h, \gamma \psi_h) = (\psi_h, \gamma \varphi_h), \quad \forall \varphi_h, \psi_h \in Y_h. \tag{20}$$

A proof of the scalar version of (20) is given in [5]. We define $|\|\mathbf{v}_h\|\|_0 = (\mathbf{v}_h, \gamma \mathbf{v}_h)$, then $\|\cdot\|_0$ and $|\|\cdot\|\|_0$ are equivalent, i.e., there exists positive constants C_1 and C_2 independent of mesh size such that

$$C_1 |\|\mathbf{v}_h\|\|_0 \le \|\mathbf{v}_h\|_0 \le C_2 |\|\mathbf{v}_h\|\|_0, \quad \forall \mathbf{v}_h \in \mathbf{X}_h. \tag{21}$$

Define the following discrete norms on $\mathbf{X}(h)$, $Y(h)$, $G(h)$, and M_h to be employed in the analysis:

$$\begin{aligned}
|\|\mathbf{v}\|\|_h^2 &= \sum_{K\in\mathcal{R}_h} |\mathbf{v}|_{1,K}^2 + \sum_{e\in\mathcal{E}^o\cup\mathcal{E}^D} h_e^{-\beta} \|[\mathbf{v}]\|_e^2,\\
|\|\psi\|\|_h^2 &= \sum_{K\in\mathcal{R}_h} |\psi|_{1,K}^2 + \sum_{e\in\mathcal{E}^o\cup\mathcal{E}^N} h_e^{-\beta} \|[\psi]\|_e^2,\\
|\|w\|\|_h^2 &= \sum_{K\in\mathcal{R}_h} |w|_{1,K}^2 + \sum_{e\in\mathcal{E}^o\cup\mathcal{E}^N} h_e^{-\beta} \|[w]\|_e^2,\\
\|q\|_0^2 &= \sum_{K\in\mathcal{R}_h} \|q\|_{0,K}^2.
\end{aligned}$$

The following trace inequality and inverse inequality to be used in later analysis can be found in [2, 5, 103, 104]. For the trace inequality, $\forall e \in \partial K$,

$$\|\mathbf{v}\|_{0,e}^2 \le C(h_K^{-1}\|\mathbf{v}\|_{0,K}^2 + h_K |\mathbf{v}|_{1,K}^2), \ \forall \mathbf{v} \in H^1(K), \tag{22}$$
$$\|\frac{\partial \mathbf{v}}{\partial \mathbf{n}}\|_{0,e}^2 \le C(h_K^{-1}|\mathbf{v}|_{1,K}^2 + h_K |\mathbf{v}|_{2,K}^2), \ \forall \mathbf{v} \in H^2(K), \tag{23}$$

and the inverse inequality, $\forall \mathbf{v}_h \in \mathbf{X}_h$

$$h|\|\mathbf{v}_h\||_h \leq C\|\mathbf{v}_h\|_0, \tag{24}$$

where C depends only on the minimum angle of $K \in \mathcal{R}_h$. The similar results are hold for variables ψ, ψ_h and w, w_h.

We proceed to multiply the momentum (2) by $\gamma \mathbf{v}_h \in \mathbf{X}_h^*$, and present the Gauss divergence theorem on each dual element $T \in \mathcal{T}_h$, then

$$\mathcal{R}\left(\frac{\partial \mathbf{u}}{\partial t}, \gamma \mathbf{v}_h\right) + \mathcal{R}\sum_{T\in\mathcal{T}_h}\int_T (\mathbf{u}\cdot\nabla)\mathbf{u}\cdot\gamma\mathbf{v}_h \,\mathrm{d}\boldsymbol{x} - \sum_{T\in\mathcal{T}_h}\int_{\partial T}(\nabla\mathbf{u}\cdot\mathbf{n})\cdot\gamma\mathbf{v}_h \,\mathrm{d}s$$
$$+\sum_{T\in\mathcal{T}_h}\int_{\partial T} p\mathbf{n}\cdot\gamma\mathbf{v}_h \,\mathrm{d}s - \mathcal{B}\sum_{T\in\mathcal{T}_h}\int_T w\nabla\varphi\cdot\gamma\mathbf{v}_h \,\mathrm{d}\boldsymbol{x} = \sum_{T\in\mathcal{T}_h}\int_T \mathbf{f}\cdot\gamma\mathbf{v}_h \,\mathrm{d}\boldsymbol{x}, \tag{25}$$

where $\mathbf{n}$ is the unit outward normal vector on ∂T. And to multiply the mass conservation (3) by $q_h \in M_h$ and integrating by parts the result over $K \in \mathcal{R}_h$, we obtain

$$\sum_{K\in\mathcal{R}_h}\int_K \nabla\cdot\mathbf{u}q_h \,\mathrm{d}\boldsymbol{x} = 0, \tag{26}$$

Multiplying the Cahn-Hilliard (4)–(5) by $\gamma\psi_h \in Y_h^*$ and $\gamma\chi_h \in G_h^*$, respectively, integrating on each dual element $T \in \mathcal{T}_h$, and taking the integration by parts, we obtain

$$\left(\frac{\partial\varphi}{\partial t}, \gamma\psi_h\right) + \sum_{T\in\mathcal{T}_h}\int_T \mathbf{u}\cdot\nabla\varphi\gamma\psi_h \,\mathrm{d}\boldsymbol{x} - L_d\sum_{T\in\mathcal{T}_h}\int_{\partial T}\nabla w\cdot\mathbf{n}\gamma\psi_h \,\mathrm{d}s = 0, \tag{27}$$
$$-\varepsilon\sum_{T\in\mathcal{T}_h}\int_{\partial T}\nabla\varphi\cdot\mathbf{n}\gamma\chi_h \,\mathrm{d}s + \frac{1}{\varepsilon}\sum_{T\in\mathcal{T}_h}\int_T f(\varphi)\gamma\chi_h \,\mathrm{d}\boldsymbol{x} = \sum_{T\in\mathcal{T}_h}\int_T w\cdot\gamma\chi_h \,\mathrm{d}\boldsymbol{x} \tag{28}$$

Let $T_j \in \mathcal{T}_h (j = 1, 2, 3)$ be the triangles in $K \in \mathcal{R}_h$, as shown in Fig. 1. Then we get

$$-\sum_{T\in\mathcal{T}_h}\int_{\partial T}(\nabla\mathbf{u}\cdot\mathbf{n})\cdot\gamma\mathbf{v}_h \,\mathrm{d}s = -\sum_{K\in\mathcal{R}_h}\sum_{j=1}^{3}\int_{\partial T_j}(\nabla\mathbf{u}\cdot\mathbf{n})\cdot\gamma\mathbf{v}_h \,\mathrm{d}s$$
$$= -\sum_{K\in\mathcal{R}_h}\sum_{j=1}^{3}\int_{A_{j+1}CA_j}(\nabla\mathbf{u}\cdot\mathbf{n})\cdot\gamma\mathbf{v}_h \,\mathrm{d}s - \sum_{K\in\mathcal{R}_h}\int_{\partial K}(\nabla\mathbf{u}\cdot\mathbf{n})\cdot\gamma\mathbf{v}_h \,\mathrm{d}s, \tag{29}$$

using the identity (19) and the fact that $[\nabla \mathbf{u}] = 0$ for $\mathbf{u} \in (H^2(\Omega))^2 \cap \mathbf{X}$ on $\mathcal{E}^o \cup \mathcal{E}^D$, we have

$$
\begin{aligned}
-\sum_{K\in\mathcal{R}_h}\int_{\partial K}(\nabla\mathbf{u}\cdot\mathbf{n})\cdot\gamma\mathbf{v}_h\,\mathrm{d}s &= -\sum_{e\in\mathcal{E}^o\cup\mathcal{E}^D}\int_e(\nabla\mathbf{u}\cdot\mathbf{n})\cdot\gamma\mathbf{v}_h\,\mathrm{d}s\\
&= -\sum_{e\in\mathcal{E}^o\cup\mathcal{E}^D}\int_e\{\nabla\mathbf{u}\}:[\gamma\mathbf{v}_h]\,\mathrm{d}s. \qquad (30)
\end{aligned}
$$

Using (18) and note that $[p] = 0$ for $p \in H^1(\Omega) \cap L_0^2(\Omega)$ on $\mathcal{E}^o \cup \mathcal{E}^D$, we obtain

$$
\sum_{T\in\mathcal{T}_h}\int_{\partial T}p\mathbf{n}\cdot\gamma\mathbf{v}_h\,\mathrm{d}s = \sum_{K\in\mathcal{R}_h}\sum_{j=1}^{3}\int_{A_{j+1}CA_j}p\mathbf{n}\cdot\gamma\mathbf{v}_h\,\mathrm{d}s + \sum_{e\in\mathcal{E}^o\cup\mathcal{E}^D}\int_e\{p\}\cdot[\gamma\mathbf{v}_h]\,\mathrm{d}s. \qquad (31)
$$

Using (18) and note that $[\nabla\varphi] = 0$ for $\varphi \in H^2(\Omega) \cap Y$ on $\mathcal{E}^o$, we obtain

$$
\begin{aligned}
-\sum_{T\in\mathcal{T}_h}\int_{\partial T}\varepsilon\nabla\varphi\cdot\mathbf{n}\gamma\chi_h\,\mathrm{d}s &= -\sum_{K\in\mathcal{R}_h}\sum_{j=1}^{3}\int_{A_{j+1}CA_j}\varepsilon\nabla\varphi\cdot\mathbf{n}\gamma\chi_h\,\mathrm{d}s\\
&\quad -\sum_{e\in\mathcal{E}^o}\int_e\varepsilon\,\{\nabla\varphi\}\cdot[\gamma\chi_h]\,\mathrm{d}s. \qquad (32)
\end{aligned}
$$

Using (18) and note that $[\nabla w] = 0$ for $\varphi \in H^2(\Omega) \cap G$ on $\mathcal{E}^o$, we obtain

$$
\begin{aligned}
-\sum_{T\in\mathcal{T}_h}\int_{\partial T}\nabla w\cdot\mathbf{n}\gamma\psi_h\,\mathrm{d}s &= -\sum_{K\in\mathcal{R}_h}\sum_{j=1}^{3}\int_{A_{j+1}CA_j}\nabla w\cdot\mathbf{n}\gamma\psi_h\,\mathrm{d}s\\
&\quad -\sum_{e\in\mathcal{E}^o}\int_e\{\nabla w\}\cdot[\gamma\psi_h]\,\mathrm{d}s. \qquad (33)
\end{aligned}
$$

Owing to (25)–(33), the weak formulation for (2)–(5) is: find $(\mathbf{u}, p, \varphi, w) \in (\mathbf{X}_h \times M_h \times Y_h \times G_h)$, such that $\forall(\mathbf{v}_h, q_h, \psi_h, \chi_h) \in (\mathbf{X}_h \times M_h \times Y_h \times G_h)$

$$
\begin{aligned}
&\mathcal{R}\left(\frac{\partial\mathbf{u}}{\partial t},\gamma\mathbf{v}_h\right) + \mathcal{R}D_1(\mathbf{u};\mathbf{u},\gamma\mathbf{v}_h) + A_1^*(\mathbf{u},\gamma\mathbf{v}_h)\\
&+B(\gamma\mathbf{v}_h,p) - \mathcal{B}D_2(w;\varphi,\gamma\mathbf{v}_h) = (\mathbf{f},\gamma\mathbf{v}_h), \qquad (34)\\
&b(\mathbf{u},q_h) = 0, \qquad (35)\\
&\left(\frac{\partial\varphi}{\partial t},\gamma\psi_h\right) + D_3(\mathbf{u};\varphi,\gamma\psi_h) + L_d A_2^*(w,\gamma\psi_h) = 0, \qquad (36)\\
&\varepsilon A_3^*(\varphi,\gamma\chi_h) + \frac{1}{\varepsilon}(f(\varphi),\gamma\chi_h) = (w,\gamma\chi_h), \qquad (37)
\end{aligned}
$$

where

$$
\begin{aligned}
A_1^*(\mathbf{u}, \gamma\mathbf{v}_h) &= -\sum_{K\in\mathcal{R}_h}\sum_{j=1}^{3}\int_{A_{j+1}CA_j}(\nabla\mathbf{u}\cdot\mathbf{n})\cdot\gamma\mathbf{v}_h\,\mathrm{d}s - \sum_{e\in\mathcal{E}^o\cup\mathcal{E}^D}\int_e\{\nabla\mathbf{u}\}:[\gamma\mathbf{v}_h]\,\mathrm{d}s,\\
A_2^*(w, \gamma\psi_h) &= -\sum_{K\in\mathcal{R}_h}\sum_{j=1}^{3}\int_{A_{j+1}CA_j}\nabla w\cdot\mathbf{n}\gamma\psi_h\,\mathrm{d}s - \sum_{e\in\mathcal{E}^o}\int_e\{\nabla w\}\cdot[\gamma\psi_h]\,\mathrm{d}s,\\
A_3^*(\varphi, \gamma\chi_h) &= -\sum_{K\in\mathcal{R}_h}\sum_{j=1}^{3}\int_{A_{j+1}CA_j}\nabla\varphi\cdot\mathbf{n}\gamma\chi_h\,\mathrm{d}s - \sum_{e\in\mathcal{E}^o}\int_e\{\nabla\varphi\}\cdot[\gamma\chi_h]\,\mathrm{d}s,\\
B(\gamma\mathbf{v}_h, p) &= \sum_{K\in\mathcal{R}_h}\sum_{j=1}^{3}\int_{A_{j+1}CA_j}p\mathbf{n}\cdot\gamma\mathbf{v}_h\,\mathrm{d}s + \sum_{e\in\mathcal{E}^o\cup\mathcal{E}^D}\int_e\{p\}\cdot[\gamma\mathbf{v}_h]\,\mathrm{d}s,\\
b(\mathbf{u}, q_h) &= \sum_{K\in\mathcal{R}_h}\int_K\nabla\cdot\mathbf{u}q_h\,\mathrm{d}\boldsymbol{x},\\
D_1(\mathbf{u};\mathbf{w}, \gamma\mathbf{v}_h) &= \sum_{T\in\mathcal{T}_h}\int_T(\mathbf{u}\cdot\nabla)\mathbf{w}\cdot\gamma\mathbf{v}_h\,\mathrm{d}\boldsymbol{x},\\
D_2(w;\varphi, \gamma\mathbf{v}_h) &= \sum_{T\in\mathcal{T}_h}\int_T w\nabla\varphi\cdot\gamma\mathbf{v}_h\,\mathrm{d}\boldsymbol{x},\\
D_3(\mathbf{u};\varphi, \gamma\psi_h) &= \sum_{T\in\mathcal{T}_h}\int_T\mathbf{u}\cdot\nabla\varphi\gamma\psi_h\,\mathrm{d}\boldsymbol{x},\\
(\mathbf{f}, \gamma\mathbf{v}_h) &= \sum_{T\in\mathcal{T}_h}\int_T\mathbf{f}\cdot\gamma\mathbf{v}_h\,\mathrm{d}\boldsymbol{x},\\
(w, \gamma\chi_h) &= \sum_{T\in\mathcal{T}_h}\int_T w\cdot\gamma\chi_h\,\mathrm{d}\boldsymbol{x}.
\end{aligned}
$$

Now, with the help of (34)–(37), we can derive the semi-discrete discontinuous finite volume element formulation for the problem (2)–(5) as follows: find $(\mathbf{u}_h, p_h, \varphi_h, w_h) \in (\mathbf{X}_h \times M_h \times Y_h \times G_h)$, such that $\forall(\mathbf{v}_h, q_h, \psi_h, \chi_h) \in (\mathbf{X}_h \times M_h \times Y_h \times G_h)$

$$
\begin{aligned}
&\mathcal{R}\left(\frac{\partial\mathbf{u}_h}{\partial t}, \gamma\mathbf{v}_h\right) + \mathcal{R}D_1(\mathbf{u}_h;\mathbf{u}_h, \gamma\mathbf{v}_h) + A_1(\mathbf{u}_h, \gamma\mathbf{v}_h)\\
&+B(\gamma\mathbf{v}_h, p_h) - \mathcal{B}D_2(w_h;\varphi_h, \gamma\mathbf{v}_h) = (\mathbf{f}, \gamma\mathbf{v}_h), \qquad (38)\\
&C(\mathbf{u}_h, q_h) = 0, \qquad (39)\\
&\left(\frac{\partial\varphi_h}{\partial t}, \gamma\psi_h\right) + D_3(\mathbf{u}_h;\varphi_h, \gamma\psi_h) + L_d A_2(w_h, \gamma\psi_h) = 0, \qquad (40)\\
&\varepsilon A_3(\varphi_h, \gamma\chi_h) + \frac{1}{\varepsilon}(f(\varphi_h), \gamma\chi_h) = (w_h, \gamma\chi_h), \qquad (41)
\end{aligned}
$$

and

$$
\begin{aligned}
A_1(\mathbf{u}_h, \gamma\mathbf{v}_h) &= A_1^*(\mathbf{u}_h, \gamma\mathbf{v}_h) + \theta \sum_{e\in\mathcal{E}^o\cup\mathcal{E}^D} \int_e \{\nabla\mathbf{v}_h\} : [\gamma\mathbf{u}_h]\,\mathrm{d}s \\
&\quad + \sum_{e\in\mathcal{E}^o\cup\mathcal{E}^D} \frac{\alpha}{h_e^\beta} \int_e [\mathbf{u}_h] : [\mathbf{v}_h]\,\mathrm{d}s, \\
A_2(w_h, \gamma\psi_h) &= A_2^*(w_h, \gamma\psi_h) + \theta \sum_{e\in\mathcal{E}^o} \int_e \{\nabla\psi_h\} \cdot [\gamma w_h]\,\mathrm{d}s \\
&\quad + \sum_{e\in\mathcal{E}^o} \frac{\alpha}{h_e^\beta} \int_e [w_h] \cdot [\psi_h]\,\mathrm{d}s, \\
A_3(\varphi_h, \gamma\chi_h) &= A_3^*(\varphi_h, \gamma\chi_h) + \theta \sum_{e\in\mathcal{E}^o} \int_e \{\nabla\chi_h\} \cdot [\gamma\varphi_h]\,\mathrm{d}s \\
&\quad + \sum_{e\in\mathcal{E}^o} \frac{\alpha}{h_e^\beta} \int_e [\varphi_h] \cdot [\chi_h]\,\mathrm{d}s, \\
C(\mathbf{u}_h, q_h) &= \sum_{K\in\mathcal{R}_h} \int_K \nabla\cdot\mathbf{u}_h q_h\,\mathrm{d}\boldsymbol{x} - \sum_{e\in\mathcal{E}^o\cup\mathcal{E}^D} \int_e \{q_h\} \cdot [\gamma\mathbf{u}_h]\,\mathrm{d}s,
\end{aligned}
$$

where $\theta = -1,\ 0$ and 1 lead to the symmetric, incomplete, and non-symmetric interior penalty formulations (SIPG, IIPG, and NIPG, respectively) in the context of interior penalty discontinuous Galerkin finite element methods. $\alpha > 0$ and $\beta > 0$ are penalty parameters [2].

Next, we present the fully discrete discontinuous finite volume element method. Let $t^j = j\Delta t$, $j = 0, 1, \ldots, N$, $\Delta t = \frac{T}{N}$, $\mathbf{u}_h^j = \mathbf{u}_h(t^j)$, $\varphi_h^j = \varphi_h(t^j)$. Combined with the backward Euler scheme in time discretization, the fully discrete discontinuous finite volume element formulation for the problem (2)–(5) is proposed as follows: find $\left\{\left(\mathbf{u}_h^{j+1}, p_h^{j+1}, \varphi_h^{j+1}, w_h^{j+1}\right)\right\}_{j=0}^{N-1} \in (\mathbf{X}_h \times M_h \times Y_h \times G_h)$, such that $\forall(\mathbf{v}_h, q_h, \psi_h, \chi_h) \in (\mathbf{X}_h \times M_h \times Y_h \times G_h)$

$$
\mathcal{R}\left(\frac{\mathbf{u}_h^{j+1} - \mathbf{u}_h^j}{\Delta t}, \gamma\mathbf{v}_h\right) + \mathcal{R}D_1(\mathbf{u}_h^{j+1}; \mathbf{u}_h^{j+1}, \gamma\mathbf{v}_h) + A_1(\mathbf{u}_h^{j+1}, \gamma\mathbf{v}_h)
$$

$$
+B(\gamma\mathbf{v}_h, p_h^{j+1}) - \mathcal{B}D_2(w_h^{j+1}; \varphi_h^{j+1}, \gamma\mathbf{v}_h) = (\mathbf{f}(t^{j+1}), \gamma\mathbf{v}_h), \tag{42}
$$

$$
C(\mathbf{u}_h^{j+1}, q_h) = 0, \tag{43}
$$

$$
\left(\frac{\varphi_h^{j+1} - \varphi_h^j}{\Delta t}, \gamma\psi_h\right) + D_3(\mathbf{u}_h^{j+1}; \varphi_h^{j+1}, \gamma\psi_h) + L_d A_2(w_h^{j+1}, \gamma\psi_h) = 0, \tag{44}
$$

$$
\varepsilon A_3(\varphi_h^{j+1}, \gamma\chi_h) + \frac{1}{\varepsilon}(f(\varphi_h^{j+1}), \gamma\chi_h) = (w_h^{j+1}, \gamma\chi_h), \tag{45}
$$

with the initial conditions $\mathbf{u}_h^0 = \mathbf{u}_{0h}$ and $\varphi_h^0 = \varphi_{0h}$. Here

$$
f_h^{j+1} = \left(\varphi_h^{j+1}\right)^3 - \varphi_h^j. \tag{46}
$$

In order to derive the basic energy law of the discrete problem, we first provide the following equivalence relations. The proof can be obtained easily by using Gauss divergence theorem on the control volumes, readers can find more details in [5, 6, 56, 57, 103, 104].

Lemma 3.2 *$\forall \mathbf{u},\ \mathbf{v} \in \mathbf{X}(h)$, $\forall \varphi,\ \psi \in Y(h)$, $\forall p,\ q \in L_0^2(\Omega)$, $\forall w,\ \chi \in G(h)$, we have*

$$
\begin{aligned}
&-\sum_{K\in\mathcal{R}_h}\sum_{j=1}^{3}\int_{A_{j+1}CA_j}\nabla\mathbf{u}\cdot\mathbf{n}\gamma\mathbf{v}\,\mathrm{d}s-\sum_{K\in\mathcal{R}_h}\sum_{j=1}^{3}\int_{A_{j+1}CA_j}\nabla w\cdot\mathbf{n}\gamma\psi\,\mathrm{d}s\\
&-\sum_{K\in\mathcal{R}_h}\sum_{j=1}^{3}\int_{A_{j+1}CA_j}\nabla\varphi\cdot\mathbf{n}\gamma\chi\,\mathrm{d}s+\sum_{K\in\mathcal{R}_h}\sum_{j=1}^{3}\int_{A_{j+1}CA_j}p\mathbf{n}\cdot\gamma\mathbf{v}\,\mathrm{d}s\\
=\ &(\nabla\mathbf{u},\nabla\mathbf{v})+\sum_{K\in\mathcal{R}_h}\int_{\partial K}\nabla\mathbf{u}\cdot\mathbf{n}(\gamma\mathbf{v}-\mathbf{v})\,\mathrm{d}s-\sum_{K\in\mathcal{R}_h}(\nabla\cdot\nabla\mathbf{u},\gamma\mathbf{v}-\mathbf{v})_K\\
&+(\nabla w,\nabla\psi)+\sum_{K\in\mathcal{R}_h}\int_{\partial K}\nabla w\cdot\mathbf{n}(\gamma\psi-\psi)\,\mathrm{d}s-\sum_{K\in\mathcal{R}_h}(\nabla\cdot\nabla w,\gamma\psi-\psi)_K\\
&+(\nabla\varphi,\nabla\chi)+\sum_{K\in\mathcal{R}_h}\int_{\partial K}\nabla\varphi\cdot\mathbf{n}(\gamma\chi-\chi)\,\mathrm{d}s-\sum_{K\in\mathcal{R}_h}(\nabla\cdot\nabla\varphi,\gamma\chi-\chi)_K\\
&+\sum_{K\in\mathcal{R}_h}\int_{K}\nabla p\cdot(\gamma\mathbf{v}-\mathbf{v})\,\mathrm{d}\boldsymbol{x}-(\nabla\cdot\mathbf{v},p)-\sum_{K\in\mathcal{R}_h}\int_{\partial K}p\mathbf{n}\cdot(\gamma\mathbf{v}-\mathbf{v})\,\mathrm{d}s,
\end{aligned}
\tag{47}
$$

if $\mathbf{u}_h,\ \mathbf{v}_h \in \mathbf{X}_h$, $\phi_h,\ \psi_h \in Y_h$, $p_h,\ q_h \in M_h$, $w_h,\ \chi_h \in G_h$, we get

$$
\begin{aligned}
&-\sum_{K\in\mathcal{R}_h}\sum_{j=1}^{3}\int_{A_{j+1}CA_j}\nabla\mathbf{u}_h\cdot\mathbf{n}\gamma\mathbf{v}_h\,\mathrm{d}s-\sum_{K\in\mathcal{R}_h}\sum_{j=1}^{3}\int_{A_{j+1}CA_j}\nabla w_h\cdot\mathbf{n}\gamma\psi_h\,\mathrm{d}s\\
&-\sum_{K\in\mathcal{R}_h}\sum_{j=1}^{3}\int_{A_{j+1}CA_j}\nabla\varphi_h\cdot\mathbf{n}\gamma\chi_h\,\mathrm{d}s+\sum_{K\in\mathcal{R}_h}\sum_{j=1}^{3}\int_{A_{j+1}CA_j}p_h\mathbf{n}\cdot\gamma\mathbf{v}_h\,\mathrm{d}s\\
=\ &(\nabla\mathbf{u}_h,\nabla\mathbf{v}_h)+(\nabla w_h,\nabla\psi_h)+(\nabla\varphi_h,\nabla\chi_h)-(\nabla\cdot\mathbf{v}_h,p_h),
\end{aligned}
\tag{48}
$$

and

$$
B(\gamma\mathbf{v}_h,q_h)=-C(\mathbf{v}_h,q_h). \tag{49}
$$

Now, the mass conservation property of the Navier-Stokes-Cahn-Hilliard system reads as follows.

Theorem 3.1 (Temporally discrete mass conservation) *Let $\left\{\left(\mathbf{u}_h^{j+1},p_h^{j+1},\varphi_h^{j+1},w_h^{j+1}\right)\right\}_{j=0}^{N-1}$ be a solution of the spatially discrete system (42)–(46). Assume that $\mathbf{f}=\mathbf{0}$, then this system has the following mass conservation*

law:

$$\int_{\Omega} \varphi_h^{j+1} \, \mathrm{d}\boldsymbol{x} = \int_{\Omega} \varphi_0 \, \mathrm{d}\boldsymbol{x}, \quad j \geq 0. \tag{50}$$

Proof Setting $\psi_h = 1$ in (44) and using Lemma 3.1 and Lemma 3.2, we have

$$\int_{\Omega} \varphi_h^{j+1} \, \mathrm{d}\boldsymbol{x} = \int_{\Omega} \varphi_h^{j} \, \mathrm{d}\boldsymbol{x}, \quad j \geq 0, \tag{51}$$

we complete the proof of Theorem 3.1. □

In the following, we prove an energy dissipation property for the Navier-Stokes-Cahn-Hilliard system.

Theorem 3.2 (Temporally discrete energy dissipation equality) *Let* $\left\{\left(\mathbf{u}_h^{j+1}, p_h^{j+1}, \varphi_h^{j+1}, w_h^{j+1}\right)\right\}_{j=0}^{N-1}$ *be the solution of the spatially discrete system* (42)-(46)*. Assume that* $\mathbf{f} = \mathbf{0}$*, then this system has the following basic energy law:*

$$\begin{aligned} E\left(t^{j+1}; \mathbf{u}^{j+1}, \varphi^{j+1}\right) - E\left(t^{j}; \mathbf{u}^{j}, \varphi^{j}\right) = & \frac{\mathcal{R}}{2} |\!|\!| \mathbf{u}_h^{j+1} |\!|\!|_0^2 + \frac{\mathcal{B}\varepsilon}{2} |\!|\!| \varphi_h^{j+1} |\!|\!|_h^2 \\ & + \frac{\mathcal{B}}{\varepsilon} F\left(\varphi_h^{j+1}\right) - \frac{\mathcal{R}}{2} |\!|\!| \mathbf{u}_h^{j} |\!|\!|_0^2 \\ & - \frac{\mathcal{B}\varepsilon}{2} |\!|\!| \varphi_h^{j} |\!|\!|_h^2 - \frac{\mathcal{B}}{\varepsilon} F(\varphi_h^{j}) \leq 0. \end{aligned} \tag{52}$$

Proof Set the test function in (42) by $\mathbf{v}_h = \Delta t \mathbf{u}_h^{j+1}$, we get

$$\begin{aligned} & \mathcal{R}\left(\frac{\mathbf{u}_h^{j+1} - \mathbf{u}_h^{j}}{\Delta t}, \Delta t \gamma \mathbf{u}_h^{j+1}\right) + \mathcal{R} D_1\left(\mathbf{u}_h^{j+1}; \mathbf{u}_h^{j+1}, \Delta t \gamma \mathbf{u}_h^{j+1}\right) + A_1\left(\mathbf{u}_h^{j+1}, \Delta t \gamma \mathbf{u}_h^{j+1}\right) \\ & + B\left(\Delta t \gamma \mathbf{u}_h^{j+1}, p_h^{j+1}\right) - \mathcal{B} D_2\left(w_h^{j+1}; \varphi_h^{j+1}, \Delta t \gamma \mathbf{u}_h^{j+1}\right) = 0. \end{aligned} \tag{53}$$

By the algebraic identity $a(a-b) = \frac{1}{2}(a^2 - b^2) + \frac{1}{2}(a-b)^2$, we have

$$\begin{aligned} \mathcal{R}\left(\mathbf{u}_h^{j+1} - \mathbf{u}_h^{j}, \gamma \mathbf{u}_h^{j+1}\right) = & \frac{\mathcal{R}}{2}\left(|\!|\!| \mathbf{u}_h^{j+1} |\!|\!|_0^2 - |\!|\!| \mathbf{u}_h^{j} |\!|\!|_0^2\right) + \frac{\mathcal{R}}{2}\left(|\!|\!| \mathbf{u}_h^{j+1} |\!|\!|_0 - |\!|\!| \mathbf{u}_h^{j} |\!|\!|_0\right)^2 \\ \geq & \frac{\mathcal{R}}{2}\left(|\!|\!| \mathbf{u}_h^{j+1} |\!|\!|_0^2 - |\!|\!| \mathbf{u}_h^{j} |\!|\!|_0^2\right). \end{aligned} \tag{54}$$

For $\mathbf{u}_h^{j+1} \in \mathbf{X}_h$, $\nabla \mathbf{u}_h^{j+1}$ is a constant on each dual element T, then

$$\mathcal{R} D_1\left(\mathbf{u}_h^{j+1}; \mathbf{u}_h^{j+1}, \Delta t \gamma \mathbf{u}_h^{j+1}\right) = \Delta t \mathcal{R} D_1\left(\mathbf{u}_h^{j+1}; \mathbf{u}_h^{j+1}, \gamma \mathbf{u}_h^{j+1}\right) = \Delta t C \mathcal{R} |\!|\!| \mathbf{u}_h^{j+1} |\!|\!|_0^2.$$

Using lemma 3.1, the equivalence of the norms $|\!|\!| \cdot |\!|\!|_0$ and $\| \cdot \|_0$, there exists $\tilde{C} > 0$ such that

$$\Delta t C \mathcal{R} |\!|\!| \mathbf{u}_h^{j+1} |\!|\!|_0^2 = \Delta t \tilde{C} \mathcal{R} \| \mathbf{u}_h^{j+1} \|_0^2 = \mathcal{R} D_1\left(\mathbf{u}_h^{j+1}; \mathbf{u}_h^{j+1}, \Delta t \mathbf{u}_h^{j+1}\right) = 0. \tag{55}$$

Using Cauchy-Schwarz and trace inequality (3.8), the well-known coercivity property of the bilinear form $A_1(\cdot,\cdot)$ satisfies

$$A_1\left(\mathbf{u}_h^{j+1}, \Delta t\gamma \mathbf{u}_h^{j+1}\right) \geq \Delta t C |\|\mathbf{u}_h^{j+1}\||_h^2. \tag{56}$$

Set the test function in (43) by $q_h = \Delta t p_h^{j+1}$, we get

$$C\left(\mathbf{u}_h^{j+1}, \Delta t p_h^{j+1}\right) = 0. \tag{57}$$

Set the test function in (44) by $\psi_h = \mathcal{B}\Delta t w_h^{j+1}$, we get

$$\begin{aligned}\left(\frac{\varphi_h^{j+1}-\varphi_h^j}{\Delta t}, \mathcal{B}\Delta t\gamma w_h^{j+1}\right) &+ D_3\left(\mathbf{u}_h^{j+1}; \varphi_h^{j+1}, \mathcal{B}\Delta t\gamma w_h^{j+1}\right)\\ &+ L_d A_2\left(w_h^{j+1}, \mathcal{B}\Delta t\gamma w_h^{j+1}\right) = 0.\end{aligned} \tag{58}$$

Similar to $A_1(\cdot,\cdot)$, we obtain

$$L_d A_2\left(w_h^{j+1}, \mathcal{B}\Delta t\gamma w_h^{j+1}\right) \geq \mathcal{B} L_d \Delta t C |\|w_h^{j+1}\||_h^2. \tag{59}$$

x Set the test function in (45) by $\chi = \mathcal{B}\gamma(\varphi_h^{j+1} - \varphi_h^j)$, we get

$$\varepsilon A_3\left(\varphi_h^{j+1}, \mathcal{B}\gamma\left(\varphi_h^{j+1}-\varphi_h^j\right)\right) + \frac{1}{\varepsilon}\left(f_h^{j+1}, \mathcal{B}\gamma\left(\varphi_h^{j+1}-\varphi_h^j\right)\right) = \left(w_h^{j+1}, \mathcal{B}\gamma\left(\varphi_h^{j+1}-\varphi_h^j\right)\right). \tag{60}$$

Define the backward difference operator

$$d_t := \frac{\varphi_h^{j+1}-\varphi_h^j}{\Delta t},\ j = 0, 1, 2, \cdots, N-1.$$

Define the auxiliary bilinear forms $A_3^s(\cdot,\cdot)$ as follows:

$$\begin{aligned}A_3^s(\varphi,\chi) = (\nabla\varphi, \nabla\chi) &- \sum_{e\in\mathcal{E}^o}\int_e \{\nabla\varphi\}\cdot[\chi]\,\mathrm{d}s\\ &+\theta\sum_{e\in\mathcal{E}^o}\int_e \{\nabla\chi\}\cdot[\varphi]\,\mathrm{d}s + \sum_{e\in\mathcal{E}^o}\frac{\alpha}{h_e^\beta}\int_e [\varphi]\cdot[\chi]\,\mathrm{d}s.\end{aligned}$$

Using lemma 3.1 and lemma 3.2, we have

$$\begin{aligned}A_3(\varphi,\gamma\chi) - A_3^s(\varphi,\chi) = &-\sum_{e\in\mathcal{E}^o}\int_e \{\nabla\varphi\}\cdot[\gamma\chi-\chi]\,\mathrm{d}s\\ &+\theta\sum_{e\in\mathcal{E}^o}\int_e \{\nabla\chi\}\cdot[\gamma\varphi-\varphi]\,\mathrm{d}s = 0.\end{aligned}$$

Then we can get

$$\begin{aligned}\varepsilon A_3\left(\varphi_h^{j+1}, \mathcal{B}\gamma\left(\varphi_h^{j+1}-\varphi_h^j\right)\right) &= \mathcal{B}\varepsilon A_3^s\left(\varphi_h^{j+1}, \varphi_h^{j+1}-\varphi_h^j\right)\\ &= \Delta t\mathcal{B}\varepsilon A_3^s\left(\varphi_h^{j+1}, d_t\varphi_h^{j+1}\right).\end{aligned} \tag{61}$$

By the algebraic identity $a(a-b)=\frac{1}{2}\left(a^2-b^2\right)+\frac{1}{2}(a-b)^2\geq\frac{1}{2}a^2-\frac{1}{2}b^2$, we have

$$\Delta t\mathcal{B}\varepsilon A_3^s\left(\varphi_h^{j+1},d_t\varphi_h^{j+1}\right)\geq\frac{\mathcal{B}\varepsilon}{2}|\|\varphi_h^{j+1}\||_h^2-\frac{\mathcal{B}\varepsilon}{2}|\|\varphi_h^j\||_h^2. \tag{62}$$

Note that $|f(\varphi)|\leq C$, we have

$$\begin{aligned}\frac{1}{\varepsilon}\left(f_h^{j+1},\mathcal{B}\gamma\left(\varphi_h^{j+1}-\varphi_h^j\right)\right)&=\frac{\mathcal{B}}{\varepsilon}\left(f_h^{j+1},\gamma\left(\varphi_h^{j+1}-\varphi_h^j\right)\right)\\&=\frac{\mathcal{B}}{\varepsilon}\left(f_h^{j+1},\varphi_h^{j+1}-\varphi_h^j\right)\\&\quad+\frac{\mathcal{B}}{\varepsilon}\left(f_h^{j+1},\gamma\varphi_h^{j+1}-\varphi_h^{j+1}-\left(\gamma\varphi_h^j-\varphi_h^j\right)\right)\\&\geq\Delta t\frac{\mathcal{B}}{\varepsilon}\left(f_h^{j+1},d_t\varphi_h^{j+1}\right).\end{aligned} \tag{63}$$

Since

$$\begin{aligned}f_h^{j+1}&=\left(\varphi_h^{j+1}\right)^3-\varphi_h^j\\&=\varphi_h^{j+1}\left(|\varphi_h^{j+1}|^2-1\right)+\Delta td_t\varphi_h^{j+1}\\&=\frac{1}{2}\left(\left(\varphi_h^{j+1}+\varphi_h^j\right)+\Delta td_t\varphi_h^{j+1}\right)\left(|\varphi_h^{j+1}|^2-1\right)+\Delta td_t\varphi_h^{j+1},\end{aligned} \tag{64}$$

then

$$\begin{aligned}\Delta t\frac{\mathcal{B}}{\varepsilon}\left(f_h^{j+1},d_t\varphi_h^{j+1}\right)&\geq\frac{\mathcal{B}\Delta t}{4\varepsilon}d_t\|\left(|\varphi_h^{j+1}|^2-1\right)\|^2+\frac{\mathcal{B}\Delta t^2}{4\varepsilon}\|d_t\left(|\varphi_h^{j+1}|^2-1\right)\|^2\\&\quad+\frac{\mathcal{B}\Delta t^2}{2\varepsilon}\|d_t\varphi_h^{j+1}\|^2\\&=\frac{\mathcal{B}}{\varepsilon}\left(F\left(\varphi_h^{j+1}\right)-F\left(\varphi_h^j\right)\right)+\frac{\mathcal{B}\Delta t^2}{4\varepsilon}\|d_t\left(|\varphi_h^{j+1}|^2-1\right)\|^2\\&\quad+\frac{\mathcal{B}\Delta t^2}{2\varepsilon}\|d_t\varphi_h^{j+1}\|^2\\&\geq\frac{\mathcal{B}}{\varepsilon}\left(F\left(\varphi_h^{j+1}\right)-F\left(\varphi_h^j\right)\right).\end{aligned} \tag{65}$$

Using (21), we have

$$-\mathcal{B}D_2\left(w_h^{j+1};\varphi_h^{j+1},\Delta t\gamma\mathbf{u}_h^{j+1}\right)+D_3\left(\mathbf{u}_h^{j+1};\varphi_h^{j+1},\mathcal{B}\Delta t\gamma w_h^{j+1}\right)=0, \tag{66}$$

$$\left(\frac{\varphi_h^{j+1}-\varphi_h^j}{\Delta t},\mathcal{B}\Delta t\gamma w_h^{j+1}\right)=\left(w_h^{j+1},\mathcal{B}\gamma\left(\varphi_h^{j+1}-\varphi_h^j\right)\right). \tag{67}$$

Together with (53)–(67), we obtain

$$\begin{aligned}&\frac{\mathcal{R}}{2}\|\mathbf{u}_h^{j+1}\|_0^2-\frac{\mathcal{R}}{2}\|\mathbf{u}_h^j\|_0^2+\frac{\mathcal{B}\varepsilon}{2}|\|\varphi_h^{j+1}\||_h^2-\frac{\mathcal{B}\varepsilon}{2}|\|\varphi_h^j\||_h^2+\frac{\mathcal{B}}{\varepsilon}\left(F\left(\varphi_h^{j+1}\right)-F\left(\varphi_h^j\right)\right)\\\leq&-\Delta tC|\|\mathbf{u}_h^{j+1}\||_h^2-\mathcal{B}L_d\Delta tC|\|w_h^{j+1}\||_h^2\leq0.\end{aligned} \tag{68}$$

Then we complete the proof of Theorem 3.2. □

The following a priori bounds for the phase function, chemical potential, and velocity are a direct result of the discrete energy dissipation law.

Theorem 3.3 *Let* $\left\{\left(\mathbf{u}_h^j, p_h^j, \varphi_h^j, w_h^j\right)\right\}_{j=1}^N$ *be the solution of the spatially discrete system* (42)–(46)*. Assume that* $\mathbf{f} = \mathbf{0}$*, then for any* $1 \le l \le N$*, we have*

$$\begin{aligned}&\frac{\mathcal{R}}{2}|\|\mathbf{u}_h^l\||_0^2+\frac{\mathcal{B}\varepsilon}{2}|\|\varphi_h^l\||_h^2+\frac{\mathcal{B}}{\varepsilon}F(\varphi_h^l)+\Delta t C\sum_{j=1}^{l}|\|\mathbf{u}_h^j\||_h^2+\mathcal{B}L_d\Delta t C\sum_{j=1}^{l}|\|w_h^j\||_h^2\\ \le\ &\frac{\mathcal{R}}{2}|\|\mathbf{u}_h^0\||_0^2+\frac{\mathcal{B}\varepsilon}{2}|\|\varphi_h^0\||_h^2+\frac{\mathcal{B}}{\varepsilon}F(\varphi_h^0).\end{aligned} \tag{69}$$

In addition, the double well potential $F(\varphi)$ *is bounded from below by a constant, then there is a positive constant* C *independent of* h *and* Δt *such that*

$$\max_{1\le j\le l}|\|\varphi_h^j\||_0^2+\max_{1\le j\le l}|\|\mathbf{u}_h^j\||_0^2<C, \tag{70}$$

$$\Delta t\sum_{1\le j\le l}|\|w_h^j\||_0^2+\Delta t\sum_{1\le j\le l}|\|\mathbf{u}_h^j\||_h^2<C. \tag{71}$$

Proof From the proof of Theorem 3.2, we know that

$$\begin{aligned}&\frac{\mathcal{R}}{2}\|\mathbf{u}_h^j\|_0^2-\frac{\mathcal{R}}{2}\|\mathbf{u}_h^{j-1}\|_0^2+\frac{\mathcal{B}\varepsilon}{2}|\|\varphi_h^j\||_h^2-\frac{\mathcal{B}\varepsilon}{2}|\|\varphi_h^{j-1}\||_h^2+\frac{\mathcal{B}}{\varepsilon}\left(F\left(\varphi_h^j\right)-F\left(\varphi_h^{j-1}\right)\right)\\ \le\ &-\Delta t C|\|\mathbf{u}_h^j\||_h^2-\mathcal{B}L_d\Delta t C|\|w_h^j\||_h^2.\end{aligned} \tag{72}$$

For any $1 \le l \le N$, take the summation of j from 1 to l, then

$$\begin{aligned}&\frac{\mathcal{R}}{2}|\|\mathbf{u}_h^l\||_0^2+\frac{\mathcal{B}\varepsilon}{2}|\|\varphi_h^l\||_h^2+\frac{\mathcal{B}}{\varepsilon}F(\varphi_h^l)+\Delta t C\sum_{j=1}^{l}|\|\mathbf{u}_h^j\||_h^2+\mathcal{B}L_d\Delta t C\sum_{j=1}^{l}|\|w_h^j\||_h^2\\ \le\ &\frac{\mathcal{R}}{2}|\|\mathbf{u}_h^0\||_0^2+\frac{\mathcal{B}\varepsilon}{2}|\|\varphi_h^0\||_h^2+\frac{\mathcal{B}}{\varepsilon}F(\varphi_h^0).\end{aligned} \tag{73}$$

In case the double well potential $F(\varphi)$ is bounded from below by a constant, since the parameters are all positive, it is straightforward to show (70)–(71) holds. □

4 Numerical examples

In this section, we present a series of numerical examples to investigate the efficiency and applicability of the presented method for the phase field model in the two-dimensional space. The fully discrete counterpart of Navier-Stokes-Cahn-Hilliard system is solved via the Newton-Raphson method with a tolerance of 10^{-6}. The iterative solver achieves convergence after at most 3 Newton steps for solving this coupled non-linear system at a given time. The first example is provided to show the

convergence and accuracy. The second and third examples test the surface tension effects of phase-field model by using the evolution of a square-shaped fluid bubble and perturbed surface of the droplet. The fourth and fifth examples test the surface tension effect and the elastic effect of the phase field model by using evolution of the two kissing bubbles and three kissing-non-kissing bubbles coalescence. The sixth example is provided to simulate the lid-driven cavity flow. In the seventh example, we use the Boussinesq approximation for phase field model to test the influence of different densities. The simulation of the viscous Rayleigh-Taylor instability was also investigated in the last example. In all of the numerical examples, we take penalty parameters $\alpha = 1000$, $\beta = 1$.

Example 1 (Convergence and accuracy). We first investigate on the numerical errors and convergence rates of the proposed method with SIPG, IIPG, and NIPG. Let the computational domain be $\Omega = [0, 1] \times [0, 1]$, choose $\mathcal{R} = \mathcal{B} = L_d = \varepsilon = 1$. The boundary condition functions and the source terms are chosen such that the following functions are the exact solutions:

$$\begin{cases} \mathbf{u} = [\sin(\pi x)\cos(\pi y), -\cos(\pi x)\sin(\pi y)]^T \sin(t), \\ p = \left(x^2 + y^2 - \frac{2}{3}\right)\cos(t), \\ \varphi = \sin(\pi x)\sin(\pi y)\sin(t). \end{cases} \tag{74}$$

We apply the proposed DFVE methods on meshes obtained by successive subdivision of Ω into uniform triangulations $\mathcal{R}_h$ of mesh sizes $h = 2^{-l}$, with $2 \le l \le 5$. Define the error by

$$e_{\mathbf{u}} = \mathbf{u} - \mathbf{u}_h, \quad e_p = p - p_h, \quad e_\varphi = \varphi - \varphi_h, \quad e_w = w - w_h.$$

In Table 1, we list the numerical errors and error of convergence (Eoc) rates with $\theta = -1, 0, 1$, and $\Delta t = 4h^2$, evolving the system until $T = 1$. It is clearly seen from Table 1 that the error estimates of $\mathbf{u}$, φ, w in L^2 norm are $O(h^2)$, the error estimates of $\mathbf{u}$, φ, w in broken H^1 norm and the error estimates of pressure p in L^2 norm are $O(h)$. The numerical results clearly show the optimal convergence rates of the present method in all of the L^2 and broken H^1 norms. From Table 1, the numerical experiments indicate that optimal error estimates in L^2 and broken H^1 norms are obtained for $\theta = 0, 1$ even with $\beta = 1$. Similar results were also observed in [56].

To achieve high numerical accuracy of phase field model at an acceptable computational cost, it is crucial to resolve the transition layer; numerical simulations [33, 88] suggest that in order to accurately capture the interfacial dynamics, at least 2–4 elements are needed across the interfacial region of thickness. Even in the context of two-dimensional simulations, using for instance $\varepsilon = 0.01$, and resolving the transition layer of thickness by means of uniform meshes can turn out to be very expensive and slow. Therefore, we utilized adaptive meshes for resolve this issue. The implementation is done in Matlab based on *iFEM* [12]. Regarding error indicators, we resort to the simplest element indicator η_K:

$$\eta_K^2 = h_K \int_{\partial K} |[\nabla \varphi]|^2 \, \mathrm{d}s, \quad \forall K \in \mathcal{R}_h. \tag{75}$$

Table 1 Numerical errors and convergence rates for example 1 with $\theta = -1, 0, 1$

θ	$\frac{1}{h}$	$\|e_{\mathbf{u}}\|$	Eoc	$\|\|e_{\mathbf{u}}\|\|_h$	Eoc	$\|e_p\|$	Eoc	$\|e_\varphi\|$	Eoc	$\|\|e_\varphi\|\|_h$	Eoc	$\|e_w\|$	Eoc	$\|\|e_w\|\|_h$	Eoc
−1	4	9.21E−2		1.14E−0		6.08E−2		1.25E−1		7.66E−1		1.41E−0		1.35E+1	
	8	3.10E−2	1.57	5.48E−1	1.06	3.05E−2	1.00	3.56E−2	1.81	3.72E−1	1.04	3.79E−1	1.89	6.94E−0	0.96
	16	8.48E−3	1.87	2.64E−1	1.06	1.52E−2	1.00	9.21E−3	1.95	1.84E−1	1.02	9.65E−2	1.97	3.50E−0	0.99
	32	2.17E−3	1.97	1.30E−1	1.02	7.62E−3	1.00	2.32E−3	1.99	9.17E−2	1.01	2.43E−2	1.99	1.75E−0	1.00
0	4	9.35E−2		1.14E−0		6.08E−2		1.25E−1		7.66E−1		1.41E−0		1.35E+1	
	8	3.16E−2	1.57	5.48E−1	1.06	3.05E−2	1.00	3.56E−2	1.81	3.72E−1	1.04	3.78E−1	1.89	6.94E−0	0.96
	16	8.64E−3	1.87	2.64E−1	1.06	1.52E−2	1.00	9.19E−3	1.95	1.84E−1	1.02	9.64E−2	1.97	3.50E−0	0.99
	32	2.21E−3	1.97	1.30E−1	1.02	7.62E−3	1.00	2.32E−3	1.99	9.16E−2	1.01	2.42E−2	1.99	1.75E−0	1.00
1	4	9.51E−2		1.15E−0		6.08E−2		1.24E−1		7.65E−1		1.40E−0		1.35E+1	
	8	3.22E−2	1.56	5.48E−1	1.06	3.05E−2	1.00	3.55E−2	1.81	3.72E−1	1.04	3.78E−1	1.90	6.94E−0	0.96
	16	8.83E−3	1.87	2.64E−1	1.06	1.52E−2	1.00	9.18E−3	1.95	1.84E−1	1.02	9.62E−2	1.97	3.50E−0	0.99
	32	2.26E−3	1.96	1.30E−1	1.02	7.62E−3	1.00	2.31E−3	1.99	9.16E−2	1.01	2.42E−2	1.99	1.75E−0	1.00

This entails using graded meshes and coarsening. At each time step, local error indicators were calculated heuristically and used to decide the refinement and coarsening process of the grid. The heuristic strategy is to refine the transition zones while coarsening the phases, for which we refer the readers to [69, 75].

In the following experiments, we only consider the SIPG method in the fully discreze scheme, namely $\theta = -1$ in (42)–(46) . For all boundaries, no-slip boundary condition for velocities and homogeneous Neumann boundary conditions for the phase parameter and the chemical potential are applied.

Example 2 (The dynamics of a square shape fluid). We simulate the evolution of a square-shaped fluid bubble in the square domain of $\Omega = [0, 1] \times [0, 1]$. Choose $\mathcal{R} = 1$, $\mathcal{B} = 12$, $L_d = 10^{-5}$, $\varepsilon = 0.01$, $\Delta t = 0.005$, $\varphi_0 = -\tanh\left(\frac{|x+y-1|+|x-y|-0.5}{\sqrt{2}\varepsilon}\right)$. Figure 2 shows the dynamic evolution of the bubble which turns to a circle under the effect of surface tension. Figure 3 shows the corresponding meshes. To illustrate that our numerical scheme (42)–(46) indeed obeys the mass conservation property and the discrete energy dissipation, the evolution of the discrete relative mass and total energy are plotted in Fig. 4a. We notice that the square bubble quickly deforms into a circular bubble while the relative mass $\left(\frac{|\int_\Omega \varphi_h^m \,\mathrm{d}\boldsymbol{x} - \int_\Omega \varphi_h^0 \,\mathrm{d}\boldsymbol{x}|}{\int_\Omega \varphi_h^0 \,\mathrm{d}\boldsymbol{x}}\right)$ remains zero in time. We also observe that the total energy is decreasing monotonically as predicted by Theorem 3.2 and tends to a constant value corresponding to a single larger drop near the equilibrium. From Fig. 4b, we observe that the volume of the drop in the entire domain is preserved well. Next, we demonstrate the effect of ε on the mass of each phase. Figures 5 and 6 show the dynamic evolution of the bubble which turns to a circle and the corresponding meshes with $\varepsilon = 0.1$. Figure 7 shows the simulation results for $\epsilon = 0.01$ and $\epsilon = 0.1$, respectively. We can see that the total mass (the integral of φ_h^m over Ω) remains constant and the relative mass remains zero during the evolution in Fig. 7a, which verifies that our method is conservative with $\epsilon = 0.01$. In addition, we plot the mass errors $\int_\Omega \varphi_h^m \,\mathrm{d}\boldsymbol{x} - \int_\Omega \varphi_h^0 \,\mathrm{d}\boldsymbol{x}$ of each phase with $\epsilon = 0.1$ in Fig. 8, which shows that the mass diffusion does occur with big ϵ during the evolution.

Example 3 (Relaxation to a disk). We simulate the evolution of perturbed surface of the droplet in the square domain of $\Omega = [0, 1] \times [0, 1]$. Choose $\mathcal{R} = 1$, $\mathcal{B} = 12$, $L_d = 10^{-5}$, $\varepsilon = 0.01$, $\Delta t = 0.005$, the initial φ_0 is given in polar coordinates (r, ϖ),

$$\boldsymbol{x} = (x, y) = (0.5 + r\cos(\varpi), 0.5 + r\sin(\varpi)) \quad 0 \le \varpi < 2\pi,$$

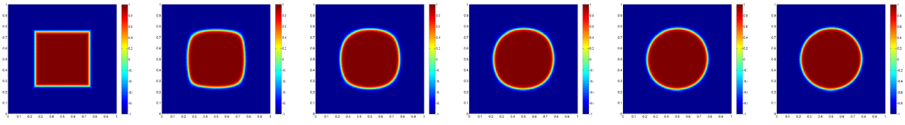

(a) $t = 0$ (b) $t = 0.05$ (c) $t = 0.1$ (d) $t = 0.15$ (e) $t = 0.2$ (f) $t = 1$

Fig. 2 The dynamics of a square shape bubble. Snapshots are shown at $t = 0, 0.05, 0.1, 0.15, 0.2, 1$

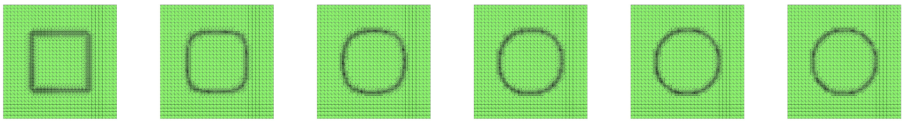

(a) $t = 0$ (b) $t = 0.05$ (c) $t = 0.1$ (d) $t = 0.15$ (e) $t = 0.2$ (f) $t = 1$

Fig. 3 Corresponding adaptively meshes at different t

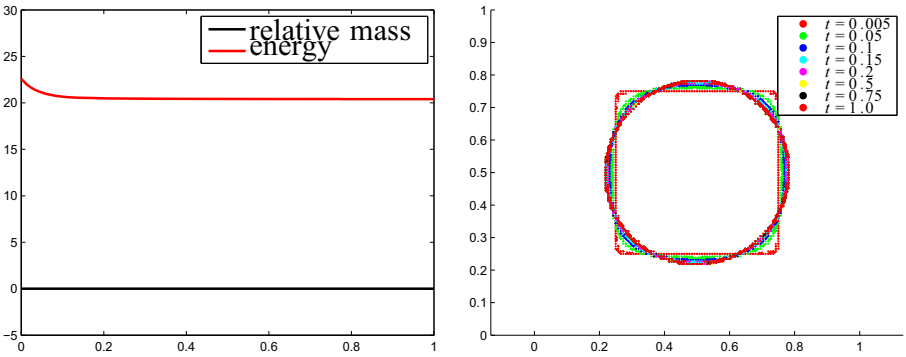

(a) Mass conservation and energy law (b) Snapshots of the zero-level set of φ

Fig. 4 The numerical mass, energy, snapshots of the zero-level set of φ with $\Delta t = 0.005$

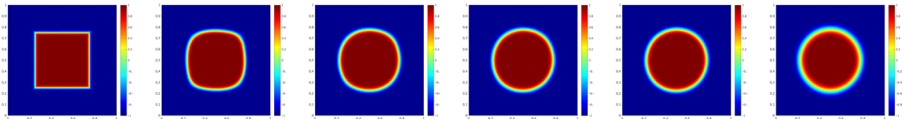

(a) $t = 0$ (b) $t = 0.05$ (c) $t = 0.1$ (d) $t = 0.15$ (e) $t = 0.2$ (f) $t = 1$

Fig. 5 The dynamics of a square shape bubble. Snapshots are shown at $t = 0, 0.05, 0.1, 0.15, 0.2, 1$ with $\epsilon = 0.1$

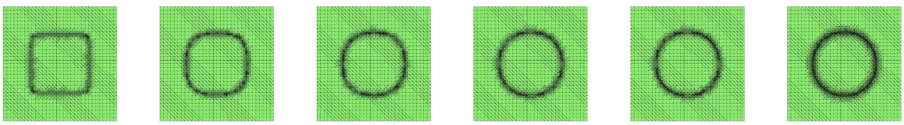

(a) $t = 0$ (b) $t = 0.05$ (c) $t = 0.1$ (d) $t = 0.15$ (e) $t = 0.2$ (f) $t = 1$

Fig. 6 Corresponding adaptively meshes at different t with $\epsilon = 0.1$

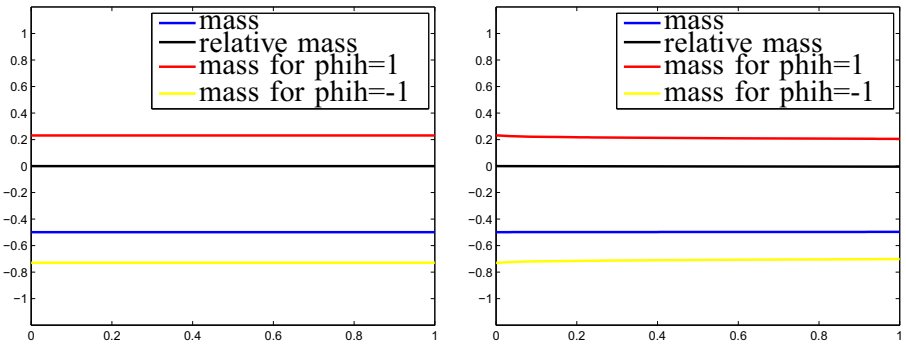

(a) $\epsilon = 0.01$ (b) $\epsilon = 0.1$

Fig. 7 The mass, relative mass, and mass of each phase with $\epsilon = 0.01$ and $\epsilon = 0.1$

where $r = 0.25 + 0.1\cos(n\varpi)$ and n is the oscillation mode. The computations are carried out for three different modes of $n = 3$, 5, and 8 (see the first picture of Figs. 9, 12, and 15, respectively). Figures 9, 10, and 11 show the dynamic evolution of the bubble which turns to a circle under the effect of surface tension, the corresponding meshes, the evolution of the discrete relative mass and total energy at different time steps, and zero-level set plots of the computed phase function for $n = 3$, respectively. For the modes of $n = 5$ and 8, the similar results are listed in Figs. 12, 13, 14, 15, 16, and 17. As we expected, all three modes of the interfaces relaxed to a circle with the same area. We also see that the larger the mode is, the more quickly the interface relaxes to a circle because of the effect of the higher curvature of the interface. In addition, through the experimental data fitting, one can obtain the rate of decrease of the total energy, which is an exponential change with respect to n.

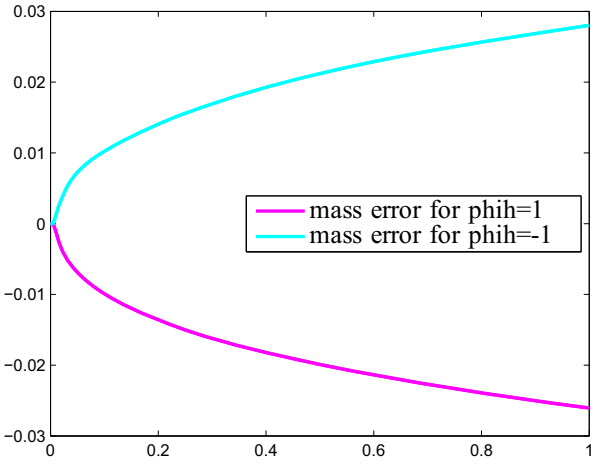

Fig. 8 The mass errors ($\int_\Omega \varphi_h^m \, d\boldsymbol{x} - \int_\Omega \varphi_h^0 \, d\boldsymbol{x}$) of each phase with $\epsilon = 0.1$

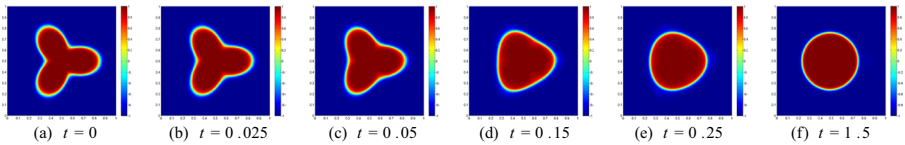

Fig. 9 Phase evolution at $t = 0, 0.025, 0.05, 0.15, 0.25, 1.5$

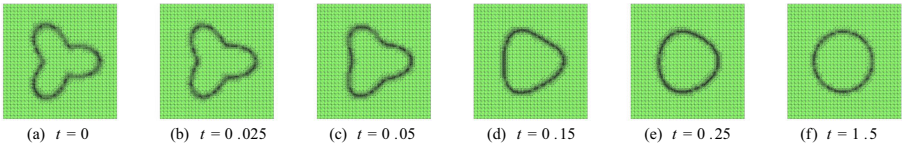

Fig. 10 Corresponding adaptively meshes at different t

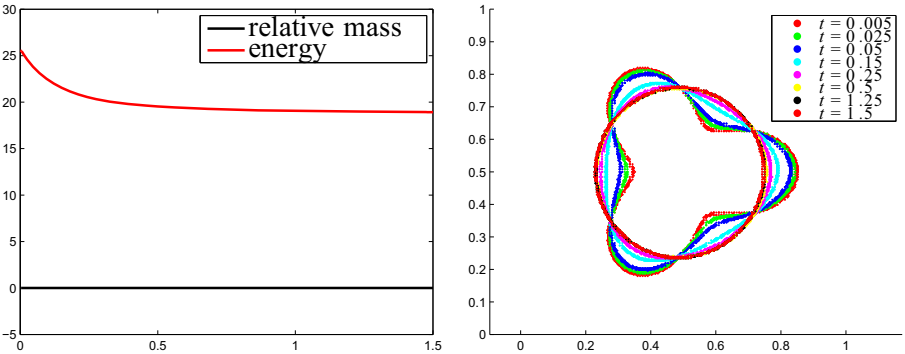

(a) Mass conservation and energy law (b) Snapshots of the zero-level set of φ

Fig. 11 The numerical mass, energy, snapshots of the zero-level set of φ with $\Delta t = 0.005$

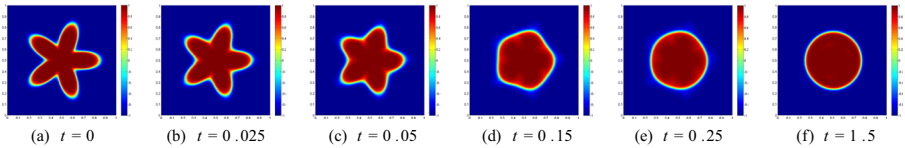

Fig. 12 Phase evolution at $t = 0, 0.025, 0.05, 0.15, 0.25, 1.5$

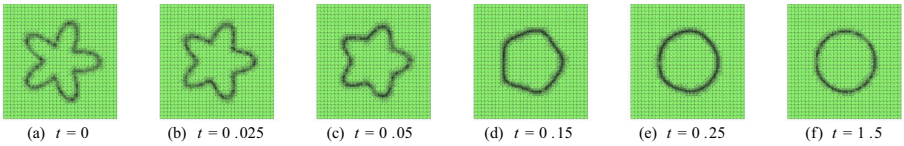

Fig. 13 Corresponding adaptively meshes at different t

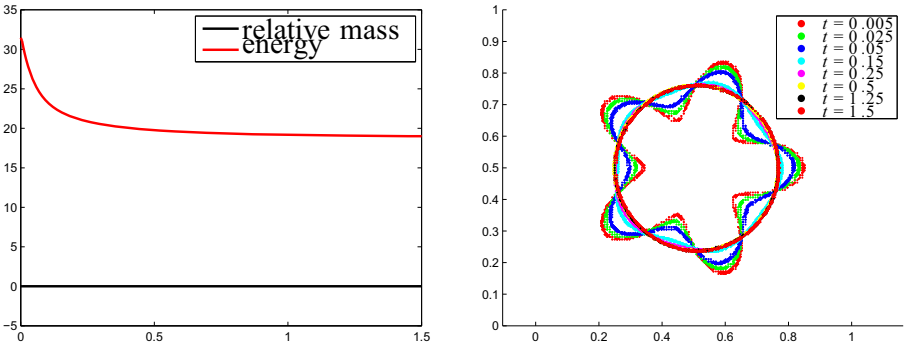

(a) Mass conservation and energy law (b) Snapshots of the zero-level set of φ

Fig. 14 The numerical mass, energy, snapshots of the zero-level set of φ with $\Delta t = 0.005$

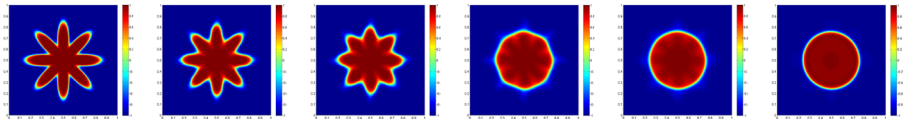

(a) $t = 0$ (b) $t = 0.025$ (c) $t = 0.05$ (d) $t = 0.15$ (e) $t = 0.25$ (f) $t = 1.5$

Fig. 15 Phase evolution at $t = 0, 0.025, 0.05, 0.15, 0.25, 1.5$

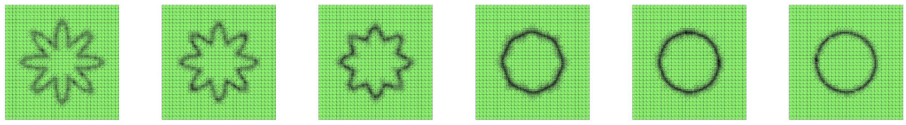

(a) $t = 0$ (b) $t = 0.025$ (c) $t = 0.05$ (d) $t = 0.15$ (e) $t = 0.25$ (f) $t = 1.5$

Fig. 16 Corresponding adaptively meshes at different t

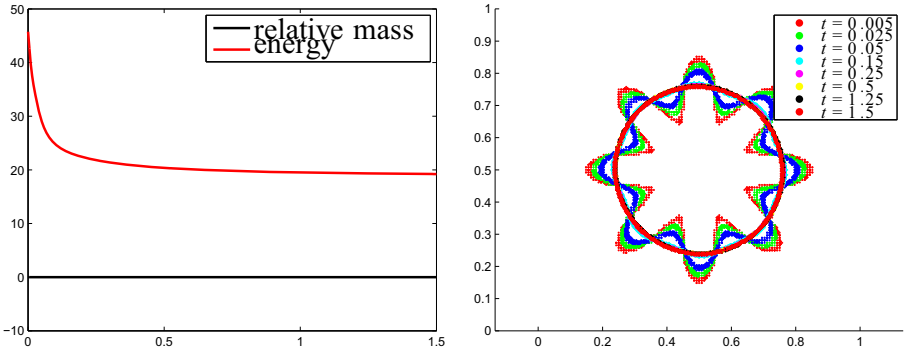

(a) Mass conservation and energy law (b) Snapshots of the zero-level set of φ

Fig. 17 The numerical mass, energy, snapshots of the zero-level set of φ with $\Delta t = 0.005$

Example 4 (Coalescence of two kissing bubbles). Two bubbles are initially laid around the center of the square domain $\Omega = [0, 0.8] \times [0, 0.8]$, close to each other but their interfaces are not overlapped. Choose $\mathcal{R} = 1$, $\mathcal{B} = 12$, $L_d = 10^{-5}$, $\varepsilon = 0.01$, $\Delta t = 0.005$, the initial phase parameter around two bubbles is given as

$$\varphi_0 = \begin{cases} -\tanh\left(\dfrac{\sqrt{(x-0.25)^2+(y-0.4)^2}-0.15}{\sqrt{2}\varepsilon}\right) & \text{for} \quad 0 < x < 0.4, \quad 0 < y < 0.8, \\ -\tanh\left(\dfrac{\sqrt{(x-0.55)^2+(y-0.4)^2}-0.15}{\sqrt{2}\varepsilon}\right) & \text{else.} \end{cases} \tag{76}$$

Due to the diffusion of two bubbles, they coalesce into a bigger circular bubble with time, the evolution of the bubbles is visually shown in Fig. 18. Located closely, but completely separated two bubbles start to share their interfaces, form a dumbbell and ellipse shape, and eventually become a circle, located at the center of domain. Figure 19 shows the corresponding meshes. Mass conservation, total energy, and zero-level set plots of the computed phase function during the coalescence are presented in Fig. 20.

Example 5 (Two kissing bubbles and one non-kissing bubble coalescence). Two kissing bubbles are close to each other but their interfaces are not overlapped, and with a non-kissing bubble of the same size. In a square domain $\Omega = [0, 0.8] \times [0, 0.8]$, choose $\mathcal{R} = 1$, $\mathcal{B} = 12$, $L_d = 10^{-5}$, $\varepsilon = 0.01$, $\Delta t = 0.005$, the initial phase parameter around two bubbles is given as

$$\varphi_0 = \begin{cases} -\tanh\left(\dfrac{\sqrt{(x-0.3)^2+(y-0.5)^2}-0.1}{\sqrt{2}\varepsilon}\right) & \text{for} \quad 0.0 < x < 0.4, \quad 0.38 < y < 0.8, \\ -\tanh\left(\dfrac{\sqrt{(x-0.5)^2+(y-0.5)^2}-0.1}{\sqrt{2}\varepsilon}\right) & \text{for} \quad 0.4 < x < 0.8, \quad 0.38 < y < 0.8, \\ -\tanh\left(\dfrac{\sqrt{(x-0.4)^2+(y-0.25)^2}-0.1}{\sqrt{2}\varepsilon}\right) & \text{else.} \end{cases} \tag{77}$$

The two located closely bubbles first deform into a circular bubble with the invariable volume as presented in Fig. 21 d and e, then this circle and the third bubble merge into a more bigger bubble as presented in Fig. 21 as a result of the surface tension effect. Figure 22 shows the corresponding meshes. Mass conservation, total energy, and zero-level set plots of the computed phase function during the coalescence are presented in Fig. 23.

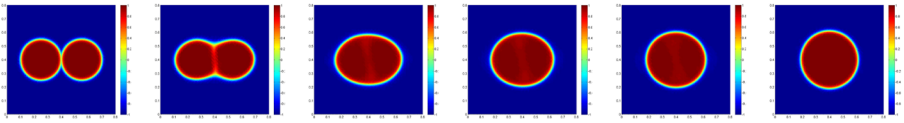

(a) $t = 0$ (b) $t = 0.5$ (c) $t = 0.25$ (d) $t = 0.35$ (e) $t = 0.5$ (f) $t = 1.5$

Fig. 18 Phase evolution at $t = 0, 0.5, 0.25, 0.35, 0.5, 1.5$

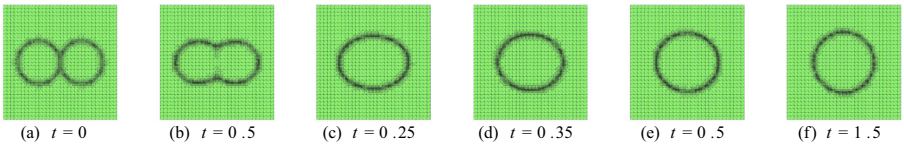

(a) $t = 0$ (b) $t = 0.5$ (c) $t = 0.25$ (d) $t = 0.35$ (e) $t = 0.5$ (f) $t = 1.5$

Fig. 19 Corresponding adaptively meshes at different t

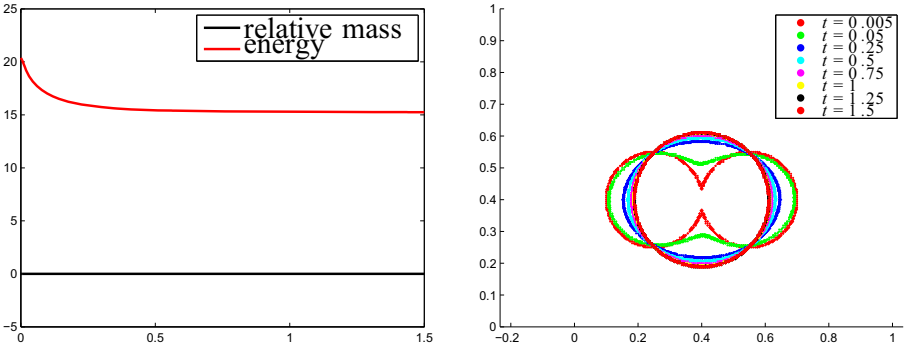

(a) Mass conservation and energy law (b) Snapshots of the zero-level set of φ

Fig. 20 The numerical mass, energy, snapshots of the zero-level set of φ with $\Delta t = 0.005$

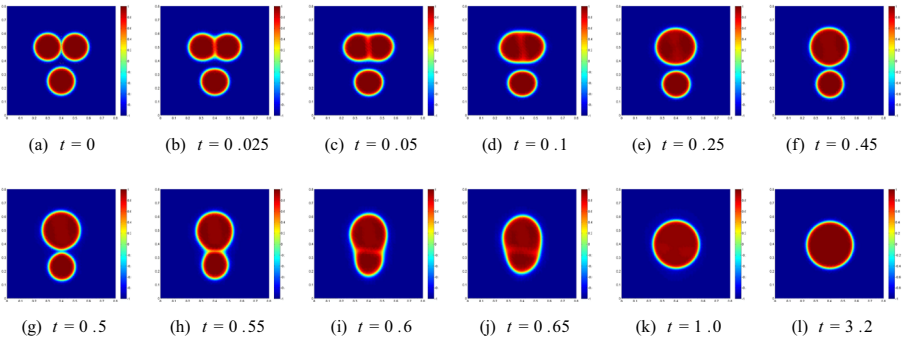

(a) $t = 0$ (b) $t = 0.025$ (c) $t = 0.05$ (d) $t = 0.1$ (e) $t = 0.25$ (f) $t = 0.45$

(g) $t = 0.5$ (h) $t = 0.55$ (i) $t = 0.6$ (j) $t = 0.65$ (k) $t = 1.0$ (l) $t = 3.2$

Fig. 21 Phase evolution at $t = 0, 0.025, 0.05, 0.1, 0.25, 0.45, 0.5, 0.55, 0.6, 0.65, 1.0, 3.2$

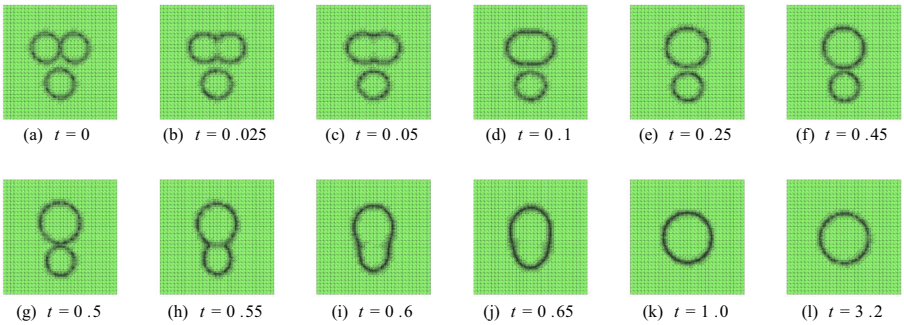

(a) $t = 0$ (b) $t = 0.025$ (c) $t = 0.05$ (d) $t = 0.1$ (e) $t = 0.25$ (f) $t = 0.45$

(g) $t = 0.5$ (h) $t = 0.55$ (i) $t = 0.6$ (j) $t = 0.65$ (k) $t = 1.0$ (l) $t = 3.2$

Fig. 22 Corresponding adaptively meshes at different t

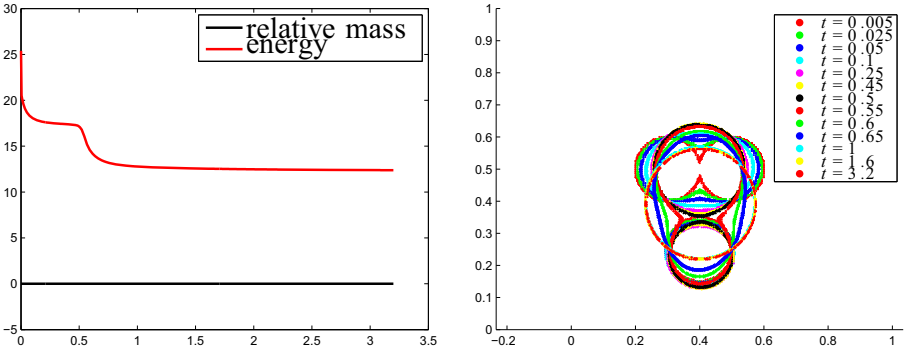

(a) Mass conservation and energy law (b) Snapshots of the zero-level set of φ

Fig. 23 The numerical mass, energy, snapshots of the zero-level set of φ with $\Delta t = 0.005$

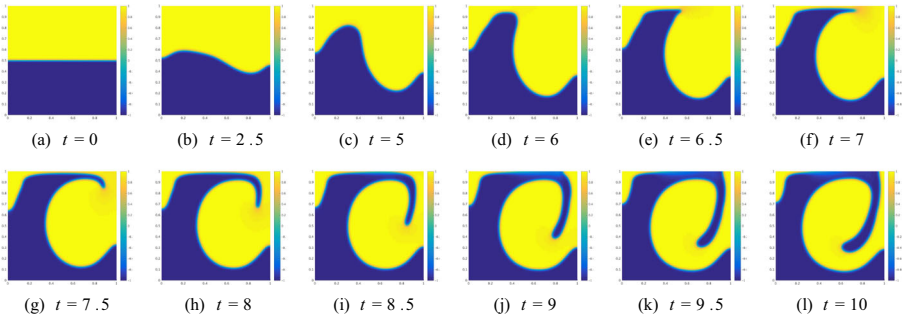

(a) $t = 0$ (b) $t = 2.5$ (c) $t = 5$ (d) $t = 6$ (e) $t = 6.5$ (f) $t = 7$

(g) $t = 7.5$ (h) $t = 8$ (i) $t = 8.5$ (j) $t = 9$ (k) $t = 9.5$ (l) $t = 10$

Fig. 24 Phase evolution at $t = 0, 2.5, 5, 6, 6.5, 7, 7.5, 8, 8.5, 9, 9.5, 10$

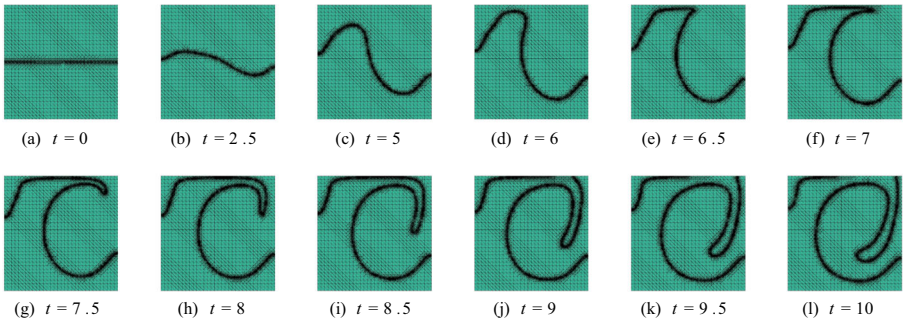

Fig. 25 Corresponding adaptively meshes at different t

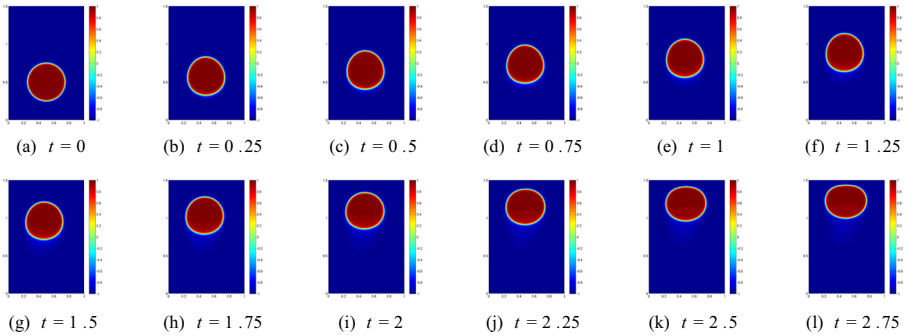

Fig. 26 Phase evolution at $t = 0, 0.25, 0.5, 0.75, 1, 1.25, 1.5, 1.75, 2, 2.25, 2.5, 2.75$

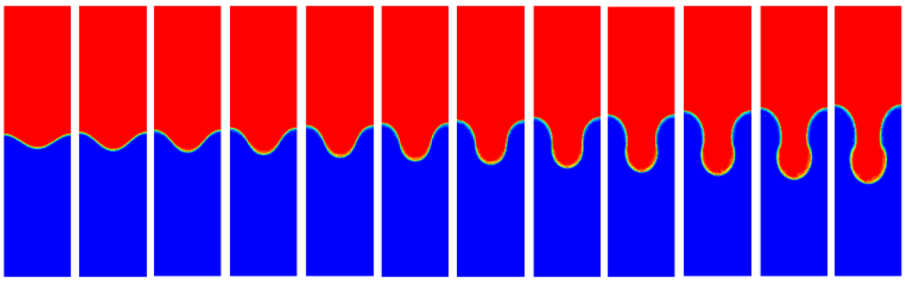

Fig. 27 Phase evolution at $t = 0, 0.2, 0.3, 0.4, 0.5, 0.6, 0.7, 0.8, 0.9, 1.0, 1.1, 1.2$ with $\nu = 0.1$

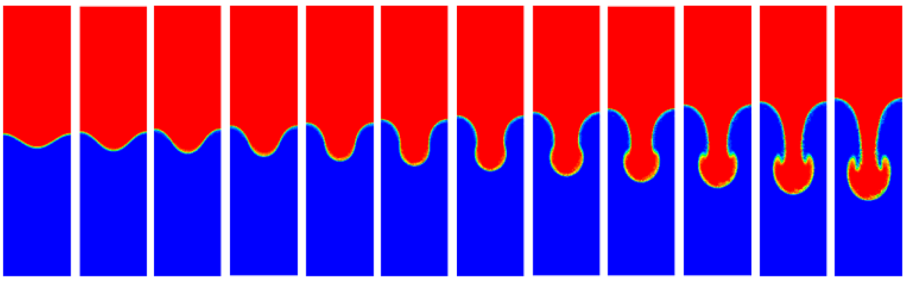

Fig. 28 Phase evolution at $t = 0, 0.2, 0.3, 0.4, 0.5, 0.6, 0.7, 0.8, 0.9, 1.0, 1.1, 1.2$ with $\nu = 0.05$

Example 6 (Lid driven cavity). This test case is based on the example proposed in [44, 52, 79], with slight modifications. We rewrite the momentum (2) as

$$\mathbf{u}_t + (\mathbf{u} \cdot \nabla)\mathbf{u} - \nu \Delta \mathbf{u} + \nabla p - \mathcal{B} w \nabla \varphi = 0 \quad \text{in } \Omega, \tag{78}$$

where constant ν is the dynamic viscosity. Let the computational domain be $\Omega = [0, 1] \times [0, 1]$. Choose $\nu = 2 \times 10^{-3}$, $\mathcal{B} = 2 \times 10^{-4}$, $L_d = 5 \times 10^{-3}$, $\varepsilon = \frac{1}{120}$, $\Delta t = 0.05$. The domain with a inflow profile $\mathbf{u} = [16x^2(x-1)^2, 0]^T$ on the top boundary and no-slip boundary conditions $\mathbf{u} = [0, 0]^T$ on the left, right and bottom boundaries. The initial phase parameter is given as a smoothed out horizontal line at $y = 0.5$: $\varphi_0 = -\tanh\left(\frac{100(y-0.5)}{\sqrt{2}\varepsilon}\right)$. The numerical results obtained from our solution procedure are shown in Figs. 24 and 25 which present the evolution of the phase function φ together with the locally refined meshes. Similar results were also observed in [44, 52, 79].

Example 7 (Boussinesq approximation). In this example, we use the classical Boussinesq approximation to phase field model where the two fluids with small density ratio [54, 67, 106]. We rewrite the momentum (2) as

$$\begin{aligned} \rho_0(\mathbf{u}_t + (\mathbf{u} \cdot \nabla)\mathbf{u}) - \nu \Delta \mathbf{u} + \nabla p - \mathcal{B} w \nabla \varphi = -(1+\varphi)\mathbf{g}(\rho_1 - \rho_0) \\ -(1-\varphi)\mathbf{g}(\rho_2 - \rho_0) \quad \text{in } \Omega, \end{aligned} \tag{79}$$

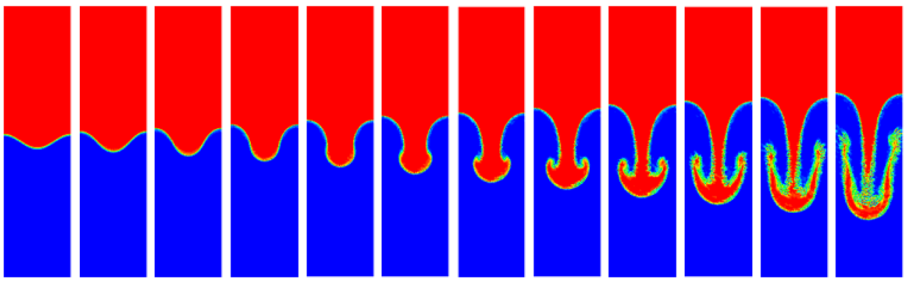

Fig. 29 Phase evolution at $t = 0, 0.2, 0.3, 0.4, 0.5, 0.6, 0.7, 0.8, 0.9, 1.0, 1.1, 1.2$ with $\nu = 0.01$

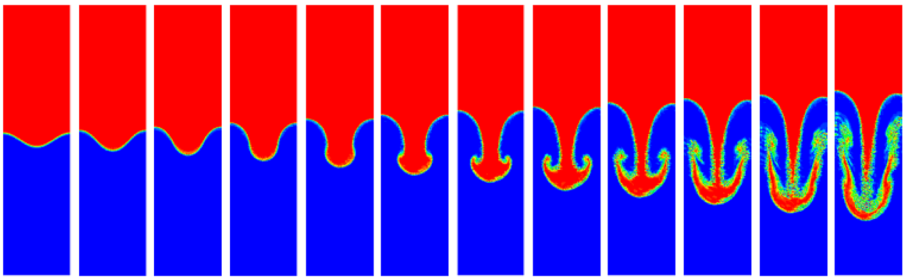

Fig. 30 Phase evolution at $t = 0, 0.2, 0.3, 0.4, 0.5, 0.6, 0.7, 0.8, 0.9, 1.0, 1.1, 1.2$ with $\nu = 0.005$

where constant ρ_0 is the "background" density contribute only to the buoyancy force, ρ_1 and ρ_2 are two immiscible, incompressible fluids density, respectively, and ν is the dynamic viscosity. We rewrite the right hand side of as

$$-(1+\varphi)\mathbf{g}(\rho_1-\rho_0)-(1-\varphi)\mathbf{g}(\rho_2-\rho_0)=-\mathbf{g}(\rho_1+\rho_2-2\rho_0)-\mathbf{g}\varphi(\rho_1-\rho_2).$$

Let the computational domain be $\Omega = [0, 1] \times [0, 1.5]$. Choose $\nu = 1$, $\mathcal{B} = 12$, $L_d = 10^{-5}$, $\varepsilon = 0.01$, $\Delta t = 0.005$, $\rho_1 = 1$, $\rho_2 = 9$, and $\rho_0 = (\rho_1 + \rho_2)/2 = 5$. The gravitational constant vector is taken to be $\mathbf{g} = [0, 10]^T$, in Fig. 26. We start with a circular bubble near the bottom of the domain. The density of the bubble is lighter than the density of the surrounding fluid, the bubble rises as expected.

Example 8 (Rayleigh-Taylor instability). In this example, we use the Boussinesq approximation to phase field model for the Rayleigh-Taylor instability. The computational domain consists of the upper high-density fluid region and the lower low-density fluid region. We assume that the interface between the two regions is smooth at the initial time and the interface evolves over time under the action of the gravitational field. We take an initial state as $\varphi_0 = \tanh\left(\frac{y-2-0.1\cos(2\pi x)}{\sqrt{2}\varepsilon}\right)$ on the computational domain $\Omega = [0, 1] \times [0, 4]$. Choose $\mathcal{B} = 0$, $L_d = 0.1$, $\varepsilon = 0.01$, $\Delta t = 0.001$, $\rho_1 = 3$, $\rho_2 = 1$, and $\rho_0 = (\rho_1 + \rho_2)/2 = 2$. The gravitational constant vector is taken to be $\mathbf{g} = [0, 10]^T$. We test the effect of $\nu = 0.1, 0.05, 0.01, 0.005$ on the solution. Figures 27, 28, 29, and 30 depict the evolution of the instability at four different values of ν. For a larger ν, the spike of the heavy fluid, no vortices are observed in the whole process, and the shear layer between the bubble and spike is stabilized due to the larger viscosity effect. In contrast, for a smaller ν, the spike of the heavy fluid first falls down and gradually rolls up, forming into two counterrotating vortices. Then these two vortices continue to grow, which results in a pair of vortices at the tails of the roll-ups. Finally, the interface undergoes a chaotic breakup, which induces the formation of an abundance of small droplets in the system.

5 Conclusions

In this paper, a fully discrete scheme combining discontinuous finite volume element methods for spatial discretization and backward Euler method for temporal discretization is proposed to solve the Navier-Stokes-Cahn-Hilliard model. The discrete energy stability is analyzed for the proposed numerical method. The features of the proposed method, such as the accuracy, mass conservation property, energy dissipation, and applicability, are demonstrated by the numerical experiments.

Funding information Rui Li is financially supported by the National Natural Science Foundation of China (11901372), the Natural Science Foundation of Shaanxi Province (2019JQ-077), and the Fundamental Research Fund for the Central Universities of China (GK201903007, GK201901008); Yali Gao is financially supported by the National Natural Science Foundation of China (11901461) and the Natural Science Foundation of Shaanxi Province (2019JQ-024); Xiaoming He is financially supported by NSF grant DMS-1818642; Jie Chen is financially supported by the XJTLU Key Programme Special Fund (KSF-P-2, KSF-E-50); Zhangxin Chen is financially supported by Foundation CMG.

References

1. Arnold, D.N.: An interior penalty finite element method with discontinuous elements. SIAM J. Numer. Anal. **19**(4), 742–760 (1982)
2. Arnold, D.N., Brezzi, F., Cockburn, B., Marini, L.D.: Unified analysis of discontinuous Galerkin methods for elliptic problems. SIAM J. Numer Anal. **39**(5), 1749–1779 (2002)
3. Bai, F., He, X., Zhou, R., Yang, X., Wang, C.: Three dimensional phase-field investigation of droplet formation in microfluidic flow focusing devices with experimental validation. Int. J Multiphase Flow **93**, 130–141 (2017)
4. Becker, R., Feng, X., Prohl, A.: Finite element approximations of the Ericksen-Leslie model for nematic liquid crystal flow. SIAM J. Numer Anal. **46**(4), 1704–1731 (2008)
5. Bi, C., Geng, J.: Discontinuous finite volume element method for parabolic problems. Numer Methods Partial Differ Equations **26**(2), 367–383 (2010)
6. Bi, C., Geng, J.: A discontinuous finite volume element method for second-order elliptic problems. Numer Methods Partial Differ Equations **28**(2), 425–440 (2012)
7. Boyer, F., Nabet, F.: A DDFV method for a Cahn-Hilliard/Stokes phase field model with dynamic boundary conditions. ESAIM Math. Model. Num. Anal. **51**, 1691–1731 (2017)
8. Bürgera, R., Kumarb, S., Ruiz-Baier, R.: Discontinuous finite volume element discretization for coupled flow-transport problems arising in models of sedimentation. J. Comput. Phys. **299**, 446–471 (2015)
9. Carstensen, C., Nataraj, N., Pani, A.K.: Comparison results and unified analysis for first-order finite volume element methods for a Poisson model problem. IMA. J. Numer. Anal. **36**(3), 1120–1142 (2016)
10. Chen, G., Hu, W., Shen, J., Singler, J., Zhang, Y., Zheng, X.: An HDG method for distributed control of convection diffusion PDEs. J. Comput. Appl. Math. **343**, 643–661 (2018)
11. Chen, J., Sun, S., Wang, X.: A numerical method for a model of two-phase flow in a coupled free flow and porous media system. J. Comput. Phys. **268**, 1–16 (2014)
12. Chen, L.: *I*FEM: An integrated finite element methods package in MATLAB. Technical report, University of California at Irvine, (2009)
13. Chen, L., Zhao, J., Yang, X.: Regularized linear schemes for the molecular beam epitaxy model with slope selection. Appl. Numer. Math. **128**, 139–156 (2018)
14. Chen, M.H., Bollada, P.C., Jimack, P.K.: Dynamic load balancing for the parallel, adaptive, multigrid solution of implicit phase-field simulations. Int. J. Numer. Anal. Mod. **16**(2), 297–318 (2019)
15. Chen, Y., Luo, Y., Feng, M.: Analysis of a discontinuous Galerkin method for the Biot's consolidation problem. Appl. Math. Comput. **219**(17), 9043–9056 (2013)

16. Chen, Y., Shen, J.: Efficient, Adaptive energy stable schemes for the incompressible Cahn-Hilliard Navier-Stokes phase-field models. J. Comput. Phys. **308**, 40–56 (2016)
17. Cheng, Y., Zhang, Q., Wang, H.: Local analysis of the local discontinuous Galerkin method with the generalized alternating numerical flux for two-dimensional singularly perturbed problem. Int. J. Numer. Anal Mod. **15**, 785–810 (2018)
18. Chessa, J., Belytschko, T.: An extended finite element method for two-phase fluids. J. Appl. Mech. (ASME) **70**, 10–17 (2003)
19. Chou, S.H., Ye, X.: Unified analysis of finite volume methods for second order elliptic problems. SIAM J. Numer. Anal. **45**(4), 1639–1653 (2007)
20. Cockburn, B., Gopalakrishnan, J., Lazarov, R.: Unified hybridization of discontinuous Galerkin, mixed, and continuous Galerkin methods for second order elliptic problems. SIAM J. Numer. Anal. **47**(2), 1319–1365 (2009)
21. Cockburn, B., Kanschat, G., Schötzau, D., Schwab, C.: Local discontinuous Galerkin methods for the Stokes system . SIAM J. Numer Anal. **40**(1), 319–343 (2002)
22. Cockburn, B., Shu, C.-W.: The local discontinuous Galerkin method for time-dependent convection-diffusion systems. SIAM J. Numer. Anal. **35**(6), 2440–2463 (1998)
23. Cui, M., Ye, X.: Unified analysis of finite volume methods for the Stokes equations. SIAM J. Numer. Anal. **48**(3), 824–839 (2010)
24. Dong, Z.: Discontinuous Galerkin methods for the Biharmonic problem on polygonal and polyhedral meshes. Int. J. Numer. Anal. Mod. **16**, 825–846 (2019)
25. Douglas, J., Dupont, T.: Interior penalty procedures for elliptic and parabolic Galerkin methods. Lect. Notes Physics **58**, 207–216 (1976)
26. Fakhari, A., Rahimian, M.H.: Phase-field modeling by the method of lattice Boltzmann equations. Phys. Rev. E. **81**, 036707 (2010)
27. Feng, X., He, Y., Liu, C.: Analysis of finite element approximations of a phase field model for two-phase fluids. Math. Comput. **76**(258), 539–571 (2007)
28. Feng, X., Karakashian, O.A.: Fully discrete dynamic mesh discontinuous Galerkin methods for the Cahn-Hilliard equation of phase transition. Math. Comp. **76**, 1093–1117 (2007)
29. Feng, X., Li, Y., Xing, Y.: Analysis of mixed interior penalty discontinuous galerkin methods for the Cahn-Hilliard equation and the Hele-Shaw flow. SIAM J. Numer. Anal **54**(2), 825–847 (2016)
30. Feng, X.B.: Fully discrete finite element approximations of the Navier-Stokes-Cahn-Hilliard diffuse interface model for two-phase fluid flows. SIAM J. Numer. Anal. **44**(3), 1049–1072 (2006)
31. Frank, F., Liu, C., Aipak, F.O., Rivière, B.: A finite volume/discontinuous Galerkin method for the advective Cahn-Hilliard equation with degenerate mobility on porous domains stemming from micro-CT imaging. Computat. Geosci. **22**(2), 543–563 (2018)
32. Fries, T.P.: The intrinsic XFEM for two-fluid flows. Int. J. Numer. Meth. Fluids **60**, 437–471 (2009)
33. Gao, M., Wang, X.P.: A gradient stable scheme for a phase field model for the moving contact line problem. J. Comput. Phys. **231**, 1372–1386 (2012)
34. Gao, M., Wang, X.P.: An efficient scheme for a phase field model for the moving contact line problem with variable density and viscosity. J. Comput. Phys. **272**, 704–718 (2014)
35. Gao, Y., He, X., Mei, L., Yang, X.: Decoupled, linear, and energy stable finite element method for the Cahn-Hilliard-Navier-Stokes-Darcy phase field model. SIAM J. Sci. Comput. **40**(1), B110–B137 (2018)
36. Girault, V., Raviart, P.A.: Finite element methods for navier-stokes equations. Theory and algorithms, Volume 5 of Springer Series in Computational Mathematics. Springer, Berlin (1986)
37. Girault, V., Rivière, B., Wheeler, M.F.: A discontinuous Galerkin method with nonoverlapping domain decomposition for the Stokes and Navier-Stokes problems. Math. Comp. **74**(249), 53–84 (2005)
38. Gunzburger, M.: Finite element methods for viscous incompressible flows. A guide to theory, practice, and algorithms. Computer Science and Scientific Computing. Academic Press, Boston (1989)
39. Han, D., Sun, D., Wang, X.: Two-phase flows in karstic geometry. Math. Method Appl. Sci. **37**(18), 3048–3063 (2013)
40. Han, D., Wang, X.: A second order in time, uniquely solvable, unconditionally stable numerical scheme for Cahn-Hilliard-Navier-Stokes equation. J. Comput. Phys. **290**, 139–156 (2015)

41. Han, D., Wang, X., Wu, H.: Existence and uniqueness of global weak solutions to a Cahn-Hilliard-Stokes-Darcy system for two phase incompressible flows in karstic geometry. J Differ. Equ. **257**(10), 3887–3933 (2014)
42. He, Q., Glowinski, R., Wang, X.P.: A least-squares/finite element method for the numerical solution of the Navier-Stokes-Cahn-Hilliard system modeling the motion of the contact line. J. Comput. Phys. **230**(12), 4991–5009 (2011)
43. He, Y., Li, L., Lanteri, S., Huang, T.Z.: Optimized Schwarz algorithms for solving time-harmonic Maxwell's equations discretized by a hybridizable discontinuous Galerkin method. Comput. Phys. Commun. **200**, 176–181 (2016)
44. Hintermüller, M., Hinze, M., Kahle, C.: An adaptive finite element Moreau-Yosida-based solver for a coupled Cahn-Hilliard/Navier-Stokes system. J. Comput. Phys. **235**, 810–827 (2013)
45. Hua, J., Linand, P., Liu, C., Wang, Q.: Energy law preserving c^0 finite element schemes for phase field models in two-phase flow computations. J. Comput. Phys. **230**, 7115–7131 (2011)
46. Huang, Q., Yang, X., He, X.: Numerical approximations for a smectic-A liquid crystal flow model: First-order, linear, decoupled and energy stable schemes. Discrete Contin. Dyn. Syst. Ser. B **23**(6), 2177–2192 (2018)
47. Jacqmin, D.: An energy approach to the continuum surface tension method. In: 34th Aerospace sciences meeting and exhibit (1996)
48. Jeon, Y., Park, E.: A hybrid discontinuous Galerkin method for elliptic problems. SIAM J. Numer. Anal. **48**(5), 1968–1983 (2010)
49. Jia, Z., Zhang, S.: A new high-order discontinuous Galerkin spectral finite element method for Lagrangian gas dynamics in two-dimensions. J. Comput. Phys. **230**(7), 2496–2522 (2011)
50. Kahle, C.: An l^∞ bound for the Cahn-hilliard equation with relaxed non-smooth free energy. Int. J. Numer. Anal. Model. **14**, 243–254 (2017)
51. Kanschat, G.: Block preconditioners for LDG discretizations of linear incompressible flow problems. J. Sci. Comput. **22**(/23), 371–384 (2005)
52. Kay, D., Styles, V., Welford, R.: Finite element approximation of a Cahn-Hilliard-Navier-Stokes system. Interfaces Free Bound **10**, 15–43 (2008)
53. R.E. Khayat: Three-dimensional boundary-element analysis of drop deformation for newtonian and viscoelastic systems. Int. J. Num. Meth. Fluids **34**, 241–275 (2000)
54. Kim, J.: Phase-field models for multi-component fluid flows. Commun. Comput. Phys. **12**(3), 613–661 (2012)
55. Kumar, S.: A mixed and discontinuous Galerkin finite volume element method for incompressible miscible displacement problems in porous media. Numer. Methods Partial Differ. Equ. **28**(4), 1354–1381 (2012)
56. Kumar, S., Nataraj, N., Pani, A.K.: Discontinuous Galerkin finite volume element methods for second-order linear elliptic problems. Numer. Methods Partial Differ. Equ. **25**, 1402–1424 (2009)
57. Kumarb, S., Ruiz-Baier, R.: Equal order discontinuous finite volume element methods for the Stokes problem. J. Sci Comput. **65**(3), 956–978 (2015)
58. Li, K., Huang, T., Li, L., Lanteri, S.: A reduced-order DG formulation based on POD method for the time-domain Maxwell's equations in dispersive media. J. Comput. Appl Math. **336**, 249–266 (2018)
59. Li, K., Huang, T., Li, L., Lanteri, S., Xu, L., Li, B.: A reduced-order discontinuous Galerkin method based on POD for electromagnetic simulation. IEEE Trans. Antenn. Propag. **66**(1), 242–254 (2018)
60. Li, K., Huang, T.-Z., Li, L., Lanteri, S.: A reduced-order discontinuous Galerkin method based on a Krylov subspace technique in nanophotonics. Appl. Math. Comput. **358**, 128–145 (2019)
61. Li, M., Guyenne, P., Li, F., Xu, L.: A positivity-preserving well-balanced central discontinuous Galerkin method for the nonlinear shallow water equations. J. Sci. Comput. **71**, 994–1034 (2017)
62. Li, R., Gao, Y., Li, J., Chen, Z.: Discontinuous finite volume element method for a coupled non-stationary Stokes-Darcy problem. J. Sci Comput. **74**(2), 693–727 (2018)
63. Lin, F., He, X.-M., Wen, X.: Fast, unconditionally energy stable large time stepping method for a new Allen-Cahn type square phase-field crystal model. Appl. Math. Lett. **92**, 248–255 (2019)
64. Lin, P., Liu, C., Zhang, H.: An energy law preserving c^0 finite element scheme for simulating the kinematic effects in liquid crystal dynamics. J. Comput. Phys. **227**(2), 1411–1427 (2007)
65. Liu, C., Frank, F., Rivière, B.: Numerical error analysis for nonsymmetric interior penalty discontinuous Galerkin method of Cahn-Hilliard equation. Numer. Methods Partial Differ. Equ. **35**(4), 1509–1537 (2019)

66. Liu, C., Rivière, B. Numerical analysis of a discontinuous Galerkin method for Cahn-Hilliard-Navier-Stokes equations arXiv:1807.02725v2 [math.NA] (2018)
67. Liu, C., Shen, J.: A phase field model for the mixture of two incompressible fluids and its approximation by a Fourier-spectral method. Physica D **179**(3-4), 211–228 (2003)
68. Liu, H., Yan, J.: The direct discontinuous Galerkin (DDG) method for diffusion with interface corrections. Commun. Comput. Phys. **8**(3), 541–564 (2010)
69. Liu, J., Mu, L., Ye, X.: An adaptive discontinuous finite volume method for elliptic problems. J. Comput. Appl. Math. **235**(18), 5422–5431 (2011)
70. Liu, J., Mu, L., Ye, X., Jari, R.: Convergence of the discontinuous finite volume method for elliptic problems with minimal regularity. J. Comput. Appl. Math. **236**(17), 4537–4546 (2012)
71. Liu, Z.H., Qiao, Z.H.: Wong-Zakai approximations of stochastic Allen-Cahn equation. Int. J. Numer. Anal. Mod. **16**, 681–694 (2019)
72. Loverich, J., Hakim, A., Shumlak, U.: A discontinuous Galerkin method for ideal two-fluid plasma equations. Commun. Comput. Phys. **9**(2), 240–268 (2011)
73. Luo, Y., Feng, M., Xu, Y.: A stabilized mixed discontinuous Galerkin method for the incompressible miscible displacement problem. Bound Value Probl. page 2011: 48 (2011)
74. Minoli, C.A.A., Kopriva, D.A.: Discontinuous Galerkin spectral element approximations on moving meshes. J. Comput. Phys. **230**(5), 1876–1902 (2011)
75. Mu, L., Jari, R.: A posteriori error analysis for discontinuous finite volume methods of elliptic interface problems. J. Comput. Appl. Math. **255**, 529–543 (2014)
76. Nguyen, N.C., Peraire, J., Cockburn, B.: An implicit high-order hybridizable discontinuous Galerkin method for the incompressible Navier-Stokes equations. J. Comput. Phys. **230**(4), 1147–1170 (2011)
77. Nishida, H., Kohashi, S., Tanaka, M.: Construction of seamless immersed boundary phase-field method. Comput. Fluids **164**, 41–49 (2018)
78. Oden, J.T., Babuska, I., Baumann, C.E.: A discontinuous Hp finite element method for diffusion problems. J. Comput. Phys. **146**, 491–519 (1998)
79. Park, K., Dorao, C.A., Fernandino, M.: Numerical solution of coupled Cahn-Hilliard and Navier-Stokes system using the least-squares spectral element method. In: Proceeding of the ICNMM conference, Washington (2016)
80. Park, K., Fernandino, M., Dorao, C.A., Gerritsma, M.: The least-squares spectral element method for phase-field models for isothermal fluid mixture. Comput. Math. Appl. **74**(8), 1981–1998 (2017)
81. Peraire, J., Persson, P.-O.: The compact discontinuous Galerkin (CDG) method for elliptic problems. SIAM J. Sci. Comput. **30**(4), 1806–1824 (2008)
82. Rayleigh, L.: On the theory of surface forces II. compressible fluids. Philos. Mag. **33**(201), 209–220 (1892)
83. Rebholz, L.G., Wise, S.M., Xiao, M.Y.: Penalty-projection schemes for the Cahn-Hilliard Navier-Stokes diffuse interface model of two phase flow, and their connection to divergence-free coupled schemes. Int. J. Numer. Anal. Mod. **15**(4-5), 649–676 (2018)
84. Repossi, E., Rosso, R., Verani, M.: A phase-field model for liquid-gas mixtures: mathematical modelling and discontinuous Galerkin discretization. Calcolo **54**, 1339–1377 (2017)
85. Rivièrem, B.: Discontinuous Galerkin Methods for Solving Elliptic and Parabolic Equations, Theory and Implementation. Society for industrial and applied mathematics philadelphia (2008)
86. Rivière, B., Wheeler, M.F., Girault, V.: Improved energy estimates for interior penalty, constrained and discontinuous Galerkin methods for elliptic problems Part 1. Comput. Geosci. **3**, 337–360 (1999)
87. Shen, J., Yang, X.: Decoupled, energy stable schemes for phase-field models of two-phase incompressible flows. SIAM J. Numer. Anal. **53**(1), 279–296 (2015)
88. Shi, Y., Bao, K., Wang, X.P.: 3D adaptive finite element method for a phase field model for moving contact line problems. Inverse Problem and Imaging **7**, 947–959 (2013)
89. Temam, R. Navier-Stokes equations. Publishing, numerical analysis. AMS Chelsea Providence, RI Reprint of the 1984 edition edition (2001)
90. van der Waals, J.: The thermodynamic theory of capillarity under the hypothesis of a continuous density variation. J. Stat. Phys. **20**, 197–244 (1893)
91. Villela, M., Villar, M., Serfaty, R., Mariano, F., Silveira-Neto, A.: Mathematical modeling and numerical simulation of two-phase flows using Fourier pseudospectral and front-tracking methods: The proposition of a new method. Appl. Math. Model. **52**, 241–254 (2017)
92. Wang, F., Han, W.: Reliable and efficient a posteriori error estimates of DG methods for a simplified frictional contact problem. Int. J. Numer. Anal. Mod. **16**, 49–62 (2019)

93. Wang, G., He, Y., Li, R.: Discontinuous finite volume methods for the stationary Stokes-Darcy problem. Int. J. Numer. Meth Engrg. **107**(5), 395–418 (2016)
94. Wang, J., Wang, Y., Ye, X.: A unified a posteriori error estimator for finite volume methods for the Stokes equations. Math. Methods Appl. Sci. **41**(3), 866–880 (2018)
95. Wang, W., Guzmán, J., Shu, C.-W.: The multiscale discontinuous Galerkin method for solving a class of second order elliptic problems with rough coefficients. Int. J. Numer. Anal. Model. **8**(1), 28–47 (2011)
96. Wheeler, M.F.: An elliptic collocation-finite element method with interior penalties. SIAM J. Numer. Anal **15**, 152–161 (1978)
97. Xia, Y., Xu, Y., Shu, C.-W.: Local discontinuous Galerkin methods for the generalized Zakharov system. J. Comput. Phys. **229**(4), 1238–1259 (2010)
98. Xu, C., Chen, C., Yang, X., He, X.-M.: Numerical approximations for the hydrodynamics coupled binary surfactant phase field model: second order, linear, unconditionally energy stable schemes. Commun. Math. Sci. **17**, 835–858 (2019)
99. Yang, J., Du, Q., Zhang, W.: Uniform $l^{p-Bound}$ of the Allen-Cahn equation and its numerical discretization. Int. J. Numer. Anal. Mod. **15**, 213–227 (2018)
100. Yang, J., Mao, S., He, X.-M., Yang, X., He, Y.: A diffuse interface model and semi-implicit energy stable finite element method for two-phase magnetohydrodynamic flows. Comput. Meth. Appl. Mech. Eng. **356**, 435–464 (2019)
101. Yang, W., Cao, L., Huang, Y.Q., Cui, J.: A new a posteriori error estimate for the interior penalty discontinuous Galerkin method. Int. J. Numer. Anal Mod. **16**, 210–224 (2019)
102. Yang, X., Zhao, J., He, X.: Linear, second order and unconditionally energy stable schemes for the viscous Cahn-Hilliard equation with hyperbolic relaxation using the invariant energy quadratization method. J. Comput. Appl. Math. **343**(1), 80–97 (2018)
103. Ye, X.: A new discontinuous finite volume method for elliptic problems. SIAM J. Numer. Anal. **42**(3), 1062–1072 (2004)
104. Ye, X.: A discontinuous finite volume method for the Stokes problems. SIAM J. Numer. Anal. **44**(1), 183–198 (2006)
105. Zhang, J., Chen, C., Yang, X., Chu, Y., Xia, Z.: Efficient, non-iterative, and second-order accurate numerical algorithms for the anisotropic Allen-Cahn Equation with precise nonlocal mass conservation. J. Comput. Appl. Math. **363**, 444–463 (2020)
106. Zhang, Z.R., Tang, H.Z.: An adaptive phase field method for the mixture of two incompressible fluids. Comput. Fluids **36**(8), 1307–1318 (2007)
107. Zheng, H., Shu, C., Chew., Y.T.: A lattice Boltzmann model for multiphase flows with large density ratio. J. Comput. Phys. **218**, 353–371 (2006)
108. Zhu, L., Huang, T., Li, L.: A hybrid-mesh hybridizable discontinuous Galerkin method for solving the time-harmonic Maxwell's equations. Appl. Math. Lett. **68**, 109–116 (2017)

Affiliations

Rui Li[1] · Yali Gao[2] · Jie Chen[3] · Li Zhang[4] · Xiaoming He[5] · Zhangxin Chen[6]

Rui Li
liruismis@snnu.edu.cn

Jie Chen
Jie.Chen01@xjtlu.edu.cn

Li Zhang
lizhang_137363@163.com

Xiaoming He
hex@mst.edu

Zhangxin Chen
zhachen@ucalgary.ca

1 School of Mathematics and Information Science, Shaanxi Normal University, Xi'an, 710119, People's Republic of China

2 School of Mathematics and Statistics, Northwestern Polytechnical University, Xi'an, 710129, People's Republic of China

3 Department of Mathematical Sciences, Xi'an Jiaotong-Liverpool University, Suzhou, 215123, People's Republic of China

4 School of Mathematical Science, University of Electronic Science and Technology of China, Chengdu, 611731, People's Republic of China

5 Department of Mathematics and Statistics, Missouri University of Science and Technology, Rolla, MO 65409, USA

6 Department of Chemical, Petroleum Engineering, Schulich School of Engineering, University of Calgary, 2500 University Drive N.W., Calgary, AB T2N 1N4, Canada